POLITECNICO
MILANO 1863

SCUOLA DI INGEGNERIA INDUSTRIALE
E DELL'INFORMAZIONE

A Reduced Order Model of Glioblastoma Growth and its Neuroimaging-informed Estimation of Patient-Specific Parameters

Tesi di Laurea Magistrale in
Mathematical Engineering - Ingegneria Matematica

Author: **Donato Cerrone**

Student ID: 977900
Advisor: Prof. Pasquale Ciarletta
Co-advisors: Davide Riccobelli, Paolo Zunino
Academic Year: 2021-22

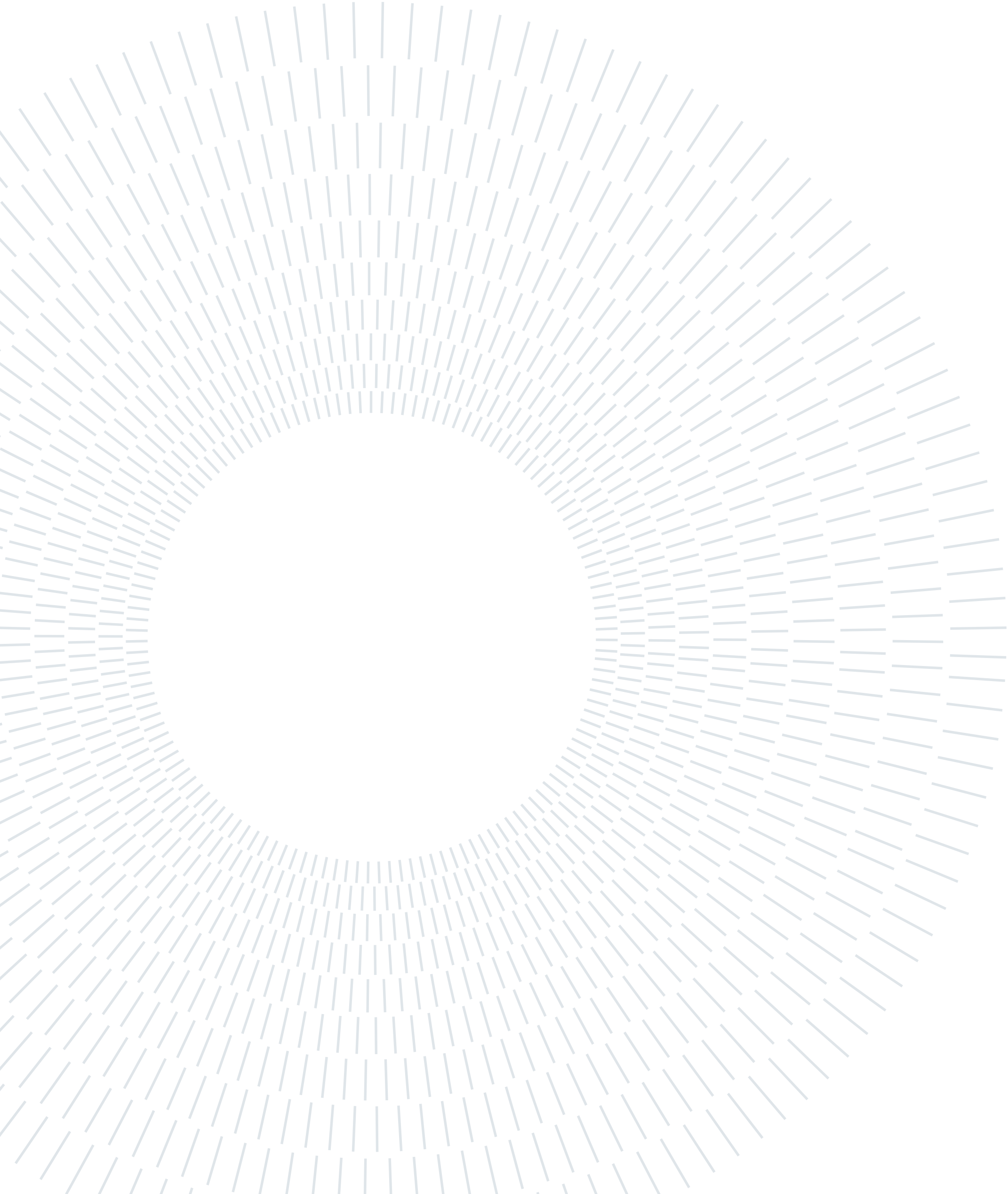

Abstract

The physical parameters driving the growth and the recurrence of Glioblastoma Multiforme (GBM) are highly specific to each patient. For this reason, finding a mathematical model that allows an accurate parameter estimation from neuroimaging data becomes of fundamental importance if we want to propose a computational framework that could help clinicians with decision-making. In general, parameter estimation requires a high computational cost, often unsuitable for clinical use if not assisted with techniques to reduce the complexity of starting problem.

In this thesis, we propose a diffuse interface model of GBM growth based on mixture theory, which consists of a Cahn-Hilliard equation coupled with a reaction-diffusion equation to describe the evolution of the nutrient for cancer cells. The specificity of each patient is modelled via a set of numerical parameters, which dictate the peculiar growth of the tumour and whose prediction is the final objective of the proposed methodology. Starting from a full-order discretization of the proposed model based on the finite element method, we obtain a reduced-base model (ROM) through the proper orthogonal decomposition technique (POD). For the solution of the PDEs system, we use `FEniCSx`, a powerful computing platform, while its reduction is computed thanks to the Python library `RBniCSx`. By means of a neural network-based approach, we build a map between the parameter space and the solution in the reduced space that describes the concentration of the tumour over time. As a tool to estimate patient-specific parameters, we propose an approach based on a second neural network trained to predict the parameters of the model based on the tumour distribution in two separate time instants. In this way, the computational effort focused on the training phase, that requires the FOM to be solved several times starting from the same initial condition, is balanced by the rapidity in the estimation of the parameters once the information on the actual evolution of the tumour at a second time instant is available. Such an approach may be exploited in clinical practice to deduce the parameters of the model from imaging data.

Keywords: Glioblastoma Multiforme, Proper Orthogonal Decomposition, Reduced Order Model, Parameters Estimation

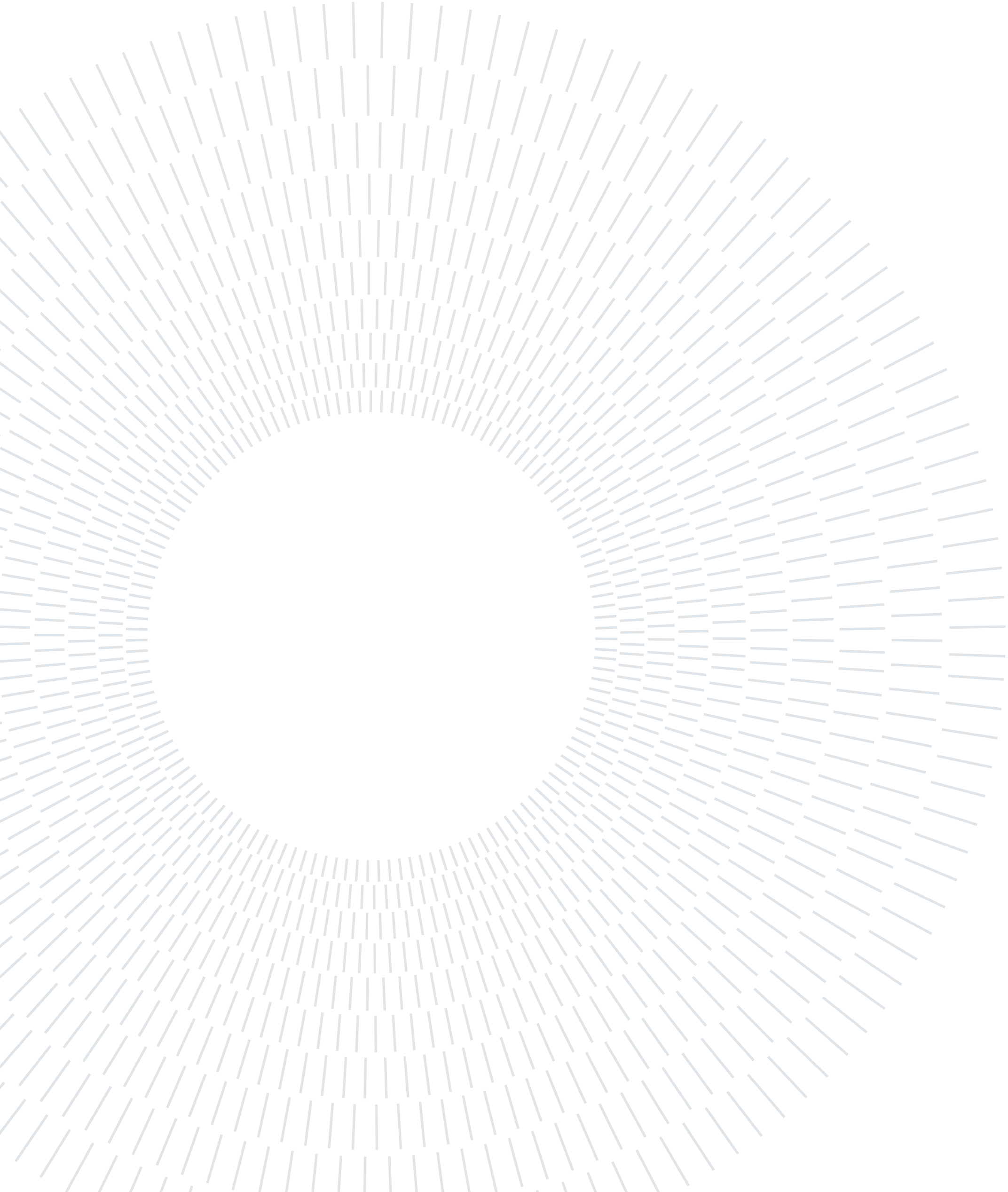

Sommario

I parametri fisici che determinano la crescita e ricomparsa del glioblastoma multiforme (GBM) sono altamente specifici per ciascun paziente. Per questo motivo, la ricerca di modelli matematici che permettano una stima adeguatamente accurata dei parametri a partire da immagini cliniche è di fondamentale importanza se si vuole aiutare il personale medico nel prendere decisioni. In generale, la stima dei parametri richiede un alto costo computazionale, spesso incompatibile per l'utilizzo clinico, se non coadiuvata a tecniche per ridurre la complessità del problema di partenza. In questa tesi, proponiamo un modello ad interfaccia diffusa per la crescita del GBM, che consiste in una equazione Cahn-Hilliard accoppiata ad un'equazione di reazione-diffusione per descrivere l'evoluzione del nutriente delle cellule tumorali. La specificità per ciascun paziente è modellata attraverso dei parametri numerici, che dettano la crescita peculiare di ciascun tumore e la cui predizione è l'obiettivo finale della metodologia proposta. Partendo da una discretizzazione full-order del modello proposta (FOM), otteniamo un modello a basi ridotte (ROM) attraverso la tecnica di *Proper Orthogonal Decomposition* (POD). Per la soluzione del sistema di PDE e la sua riduzione, utilizziamo le librerie `FEniCSx` e `RBniCSx`. Utilizzando un approccio basato su reti neurali, costruiamo una mappa tra lo spazio dei parametri e la soluzione proiettata sullo spazio ridotto che descrive la concentrazione tumorale nel tempo. Per stimare i parametri specifici del paziente, proponiamo l'utilizzo di un'ulteriore rete neurale allenata a predire i parametri del modello basandosi sulla distribuzione del tumore in due istanti di tempo distinti. In questo modo, lo sforzo computazionale concentrato nel training delle reti, che richiede che il FOM sia risolto molte volte partendo dalle medesime condizioni iniziali, è bilanciato dalla rapidità con cui i parametri vengono stimati una volta disponibile l'informazione sulla evoluzione reale del tumore ad un secondo instante temporale. Questo metodo potrebbe essere sfruttato in un caso reale per dedurre i parametri del modello dalle immagini cliniche in possesso.

Parole chiave: Glioblastoma Multiforme, Proper Orthogonal Decomposition, Reduced Order Model, Stima dei parametri.

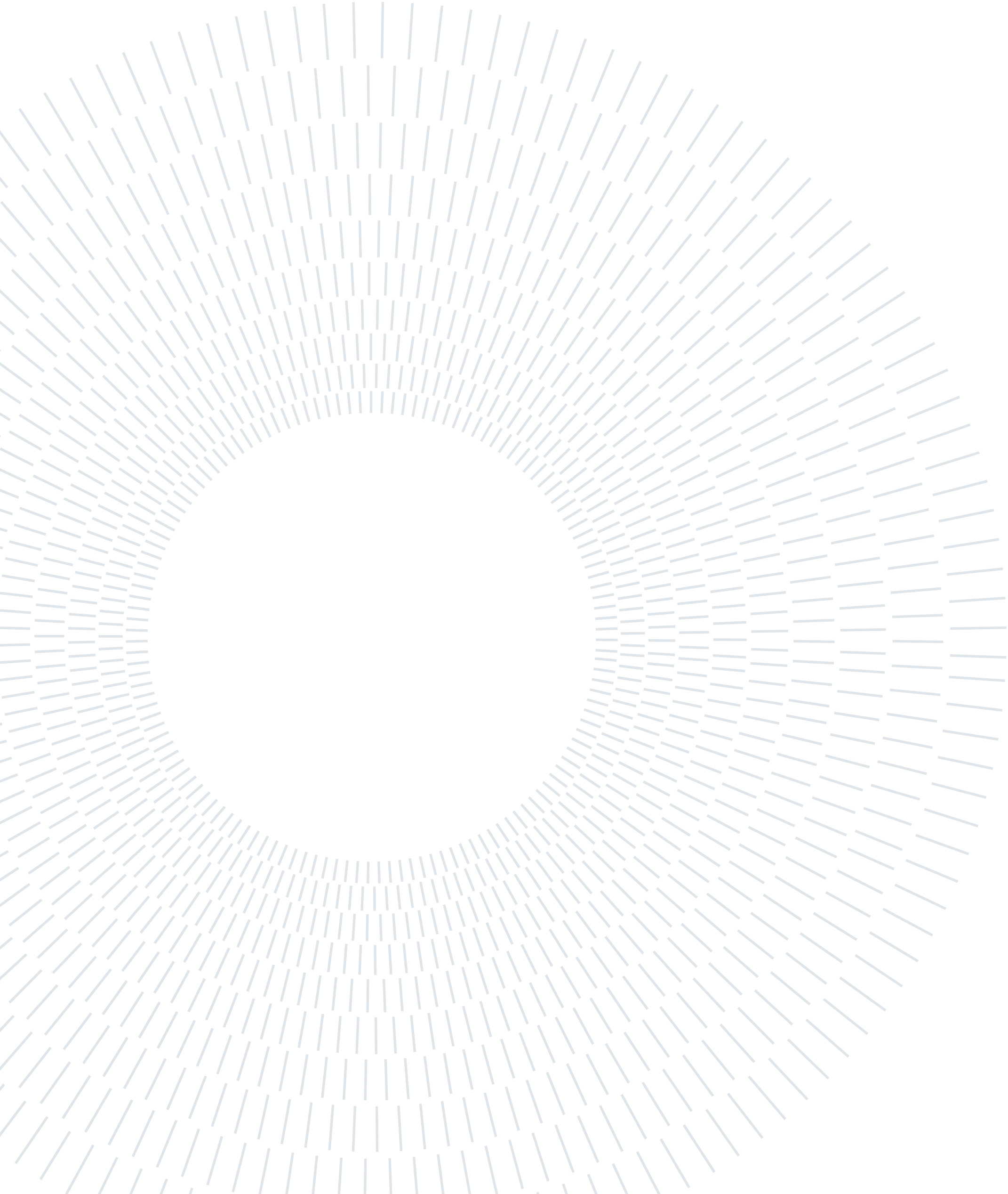

Contents

Introduction

Glioblastoma multiforme (GBM) is the most complex and deadly type of brain cancer. In addition to the typical characteristics of cancer (e.g., uncontrolled cellular proliferation, intense resistance to apoptosis, and rife genomic instability), GBM has a high invasive potential and grows along white matter fibres or vessels, imitating the physical structures of the brain's extracellular environment. The resulting diffuse infiltration and the inability of many conventional drugs to penetrate the blood-brain barrier make GBM particularly aggressive and difficult to treat. Indeed, even after extensive surgery and therapies, the median patient survival does not exceed 10 to 16 months and the five-year survival rate is approximately 5%. For these reasons, mathematical models able to describe its proliferation are of fundamental importance. Indeed, they represent an in *in silico* counterpart of the patient, which can be used to predict the evolution of the disease and the effects of treatments.

In this work, we construct a thermodynamically consistent mathematical model of GBM spreading based on mixture theory. The brain is described as a mixture of healthy and cancer cells behaving as a highly viscous fluid. The governing equations are a Cahn-Hilliard type equation, coupled with a growth term and coupled with a reaction-diffusion equation describing its nutriment behaviour. This lead to a highly non-linear system of partial differential equations that can be numerically solved by means of the finite element method.

Nonetheless, the approximation of such a problem on a 3D domain requires a huge computational effort. This can be a huge issue if we consider in addition that the tumour development, and consequently the parameter of the model are strongly patient-specific. So without further elaboration, the resolution of the model itself remains unfeasible from a clinical point of view.

To face this challenging problem, some techniques, such as the Proper Orthogonal Decomposition (POD) can be used to reduce the computational complexity. In Chapter 4 we modified the original numerical model, also called *Full Order Model* (FOM), obtaining a reduced version, the so-called *Reduced Order Model* (ROM), that keeps all the information needed to describe the evolution of the tumour over time. Indeed, it is possible to properly construct a basis of much fewer elements than the one of the FOM and still reconstruct the solution, named also *snapshot*, approximately well.

Such a simplification is of primary importance when we want to perform an estimation of patient-specific parameters. Indeed many optimization algorithms and other mathematical methods compute the solution several times in order to retrieve optimal parameters.

Here, we exploit the power of artificial neural networks to provide results in a negligible time once the networks are sufficiently trained. The problem of finding the coefficient of the ROM solution at each time-step and the parameter estimation, when a couple of snapshots are given, are both mapped through a neural network.

Finally, in Chapter 5 we present some results of the developed numerical platform. All the numerical simulations are computed via `FEniCSx`, which is a powerful computational tool for solving partial differential equations. The computational effort of the simulations phase, which can start as soon as we get information on the actual status of the patient and which includes enough simulation to train the neural networks, is balanced by the rapidity of a patient-specific prediction once we collect a second information on the evolution of the tumour growth.

For these reasons, the method presented in this work makes it possible in a realistic case to predict the future growth of the tumour making the therapy more effective.

1 | Elements of brain physiology

In this Chapter, we introduce some elements of brain physiology necessary to construct the mathematical model presented in the following Chapters. First, we provide a brief overview of the brain anatomy, emphasising the main actors involved in tumour development. Second, we describe the dynamics of tumour growth and, specifically, of the *glioblastoma multiforme*.

1.1. Brain anatomy

The brain (or *encephalon*), is one of the most complex organs in a vertebrate's body. Each human brain contains about 85 billion cells devoted to the transmission of electric signals [34]. Such cells are called *neurons*. The brain plays a key role in coordinating voluntary and involuntary actions and in the collection and transmission of signals through the body. From an anatomical point of view, the brain can be subdivided into three main regions (see Fig. 1.1).

- **Cerebrum**. It is the largest section and is composed of the right and left hemispheres. It is responsible for the interpretation of external stimuli (touch, vision, hearing, taste and smell) as well as the processing of speech, reasoning, emotions and learning, and it orchestrates movements.
- **Cerebellum**. It lies below the cerebrum and is responsible for balance, the ability to stay upright, the synchronization of motions, and the capacity for concentration;
- **Brainstem**. The brainstem can be in turn divided into the *midbrain* (or *mesencephalon*), the *pons* and the *medulla oblongata*. It is the lowest part of the brain and wires the brain to the spinal cord. The brainstem (*truncus cerebri*) controls the most elementary biological functions, including consciousness, the sleep-wake cycle, and regulation of the respiratory and circulatory systems.

As for all other organs, the brain is composed of cells that identify the peculiar role of the organ, which together form the *parenchyma* and cells whose function is to connect, support and provide nutrients for the parenchyma itself, whose collection is named *stroma*. In

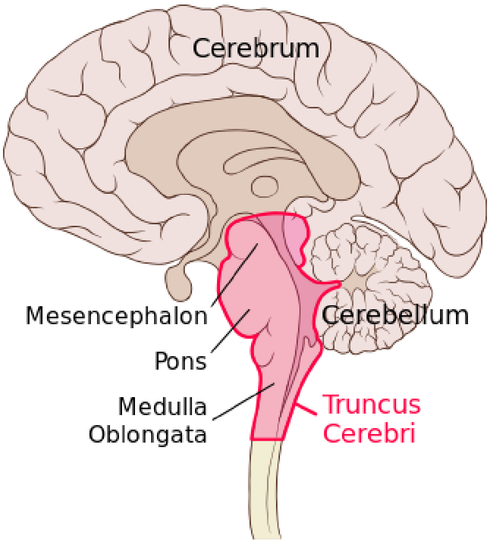

Figure 1.1: Brain anatomy: the three main sections of the human brain (cerebrum, cerebellum and brainstem). The brainstem (*truncus cerebri*) is in turn subdivided into midbrain (*mesencephalon*), pons and medulla oblongata. [3]

particular, the encephalon parenchyma consists of *neurons* and *neuroglia* whereas stroma is mostly made up of blood vessels and connective tissue.

Neurons are specialized cells, unable to reproduce themselves, but with the capability to be electrically stimulated to process and transmit information. They look like globular bodies called *soma*, from which long cable, named *axon*, and multiple filaments, *dendrites*, branch off. To be more clear, axons are long filaments that normally transmit action potentials out from the cell body. The axon's role is to convey information to various neurons, muscles, and glands. Dendrites are instead short and thickly branched in such a way that can connect with multiple axons afferent to different neurons via a biological structure called *synapses*. They serve a crucial function in integrating synaptic inputs and controlling the amount of electrical stimuli to which the neuron generates action potentials.

Neuroglia, or *glial cells*, are specialized in several ways in order to support and maintain neurons. One of their functions is to produce the *myelin sheath*, i.e. a white lipid substance that can surrounds axons to improve the conductibility of electrical signals. Axons surrounded by myelin sheaths are called *myelinated axons*.

The presence of such a substance is an indicator of different sections of the brain having specific functions. Indeed, within the brain, we can identify the so-called *white* and *grey matter*, see Fig. 1.2. White matter is mostly made up of myelinated long-range axons, while neuron bodies and dendrites mainly lie in grey matter. Grey matter is largely linked

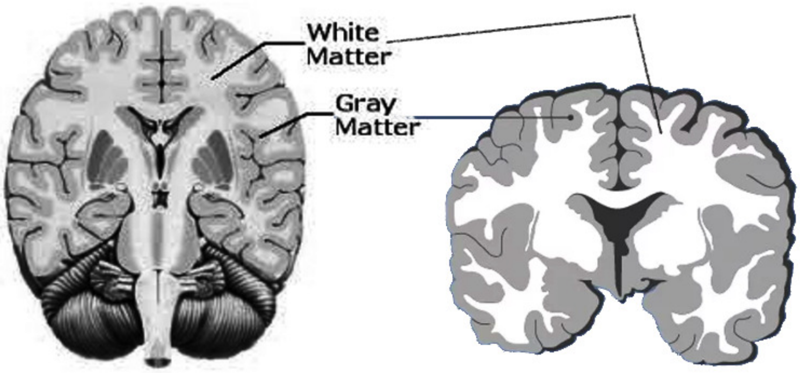

Figure 1.2: Distribution of withe and grey matter in the brain. [4]

to processing and cognition. As a coordinator of communication between various brain areas, white matter instead has the aim of modulating the dispersion of action potentials. In other words, grey matter houses the information processing centres and white matter allows the connections between these areas.

1.2. Glioblastoma multiforme

In the following, we briefly describe the pathophysiology a peculiar kind of aggressive brain cancer, the *glioblastoma multiforme.* First, we review some basic facts about tumour growth in general. Then, we enter more into detail specifying the peculiar characteristic of the glioblastoma multiforme.

1.2.1. Tumor growth

The ordinary cell life cycle ends with cell death. Such a process can be the result of *necrosis*, i.e. a traumatic cell death brought by acute cellular damage, or *apoptosis*, a form of programmed cell death which aims at controlling the number of cells in the organism. The two best-understood activation mechanisms for this phenomenon are the so-called *intrinsic pathway* and the *extrinsic pathway.* [11]

- The intrinsic pathway is activated by intracellular signals generated when cells undergo chemical stresses and depend on the release of proteins from the intermembrane space of mitochondria.
- The extrinsic pathway is activated by extracellular ligands binding to cell-surface

death receptors, which leads to the formation of the death-inducing signalling complex.

In contrast to necrosis, apoptosis is a well-controlled process that brings benefits to the organism's life cycle. Sometimes, cell apoptosis does not take place for endogenous reasons (e.g. error in cell division) or exogenous ones (smoke, chemicals, metals or pathogens). Specifically, when a mutation in the DNA occurs, the cell tries to fix it. If such a process fails, the cell tries to induce apoptosis. When even this mechanism goes wrong and the cell is able to ignore growth-inhibiting signals from its neighbours, an uncontrolled proliferation of these mutated cells takes place.

Although the process of mutation accumulation may take years to complete, many factors can speed up the process. Some of these factors are exposure to carcinogens and other harsh environmental factors able to induce DNA mutations.

The uncontrolled cell replication results in a mass of aberrant cells that may alter the surrounding microenvironment to enhance its own survival. This cascade of malfunctions is called *carcinogenesis* and leads to the formation of a *tumour*, also known as *neoplasm.* [25]

Tumours can be subdivided into benign and malignant tumours depending on the expected behaviour of the specific neoplasm. Indeed, benign neoplasms remain localized where the initial mutation took place. Conversely, malignant neoplasms may invade the surrounding tissue and, in most cases, can metastasize to distant organs [38].

To summarize what features different tumours have in common, in 2000, cancer researchers Hanahan and Weinberg [31] pointed out six hallmarks that are essential alterations in cell physiology that collectively decree malignant growth:

1. self-sufficiency in growth signals;
2. insensitivity to growth-inhibitory signals;
3. evasion of apoptosis;
4. limitless replicative potential (immortality);
5. sustained angiogenesis (the formation of new blood vessels);
6. tissue invasion and metastasis (the spread of the tumour to another organ).

Yet, in 2011, other distinct attributes of cancer cells have been proposed to be functionally important for the development of cancer and might therefore be added to the list of core hallmarks [30]. Two such attributes are particularly compelling:

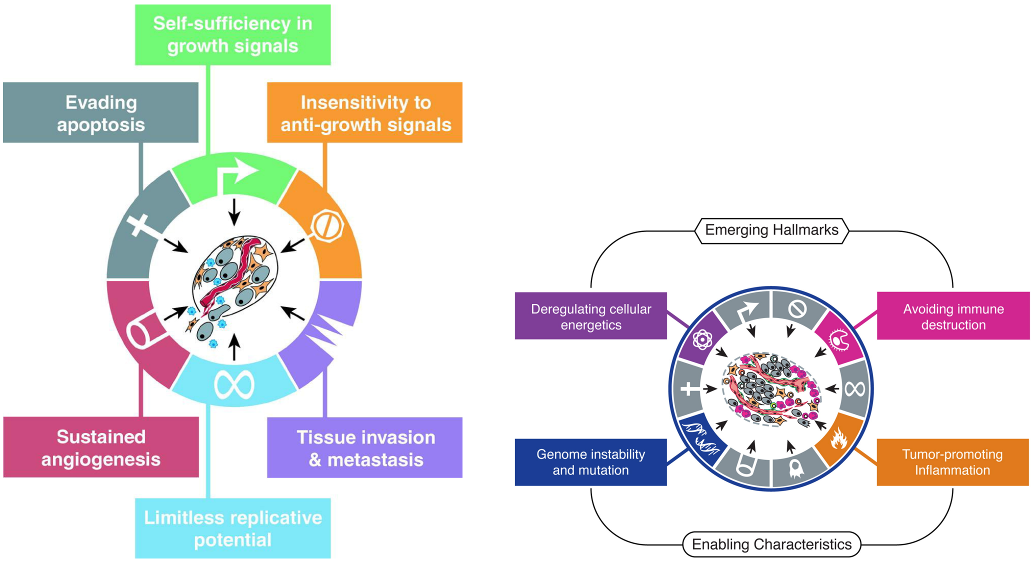

(a) (b)

Figure 1.3: Acquired Capabilities of Cancer. (a) Cancers have acquired the same set of functional capabilities during their development, albeit through various mechanistic strategies. (b) An increasing body of research suggests that two additional hallmarks of cancer are involved in the pathogenesis of some and perhaps all cancers. One involves the capability to modify or reprogram, cellular metabolism in order to most effectively support neoplastic proliferation. The second allows cancer cells to evade immunological destruction, in particular by T and B lymphocytes, macrophages, and natural killer cells.

7. capability reprogramming of cellular energy metabolism in order to support continuous cell growth and proliferation;
8. active evasion by cancer cells from attack and elimination by immune cells.

These features make the tumour a disease difficult to treat. Nowadays, cancer is the second leading cause of death globally according to the World Health Organization: worldwide, an estimated 19.3 million new cancer cases and almost ten million cancer deaths occurred in 2020 [55]. Hence, it is not difficult to understand the importance of a thorough and complete investigation of all the mechanisms involved in tumour genesis, proliferation and elimination.

1.2.2. Pathophysiology of Glioblastoma Multiforme

Glioblastoma Multiforme (GBM) is the most widespread and aggressive malignant tumour among glial neoplasms. Also known as *gliomas*, glial neoplasms are a heterogeneous group of brain tumours that originates in cerebral parenchyma starting from glial cells. In general, symptoms are different and vary according to the location manifesting as a focal neurological deficit, encephalopathy or convulsions. Gliomas, according to the World Health Organization grading system, are classified on a scale from I to IV associated with the malignity of the tumour ([39]-[27]). Each category of glioma is indeed labelled in the following way:

- Grade I: tumours in this category are characterized by a low proliferation rate. They are benign and frequently treatable by surgical excision.
- Grade II: this category includes low-aggressive tumours with a long characteristic diffusion time. These tumours are characterized by infiltration of the parenchyma. Thus, they cannot be treated only with surgery.
- Grade III: in this case, cancer cells start to lose the morphological and functional traits of the original tissue (*anaplasia*). This condition guarantees a faster proliferation of the neoplasm.
- Grade IV: these are tumours that have built their own vascular network, providing nutrients to a larger number of cells and making them more resistant to radiotherapy and chemotherapy.

In this classification, GBM is a tumour (specifically, an *astrocytic tumours*) of IV grade.

Glioblastoma represents 15% of all intracranial neoplasms and 60-75% of astrocytic tumours [60] (see Table 1.1). GMB mostly affects adults and typically develops in the cerebral hemispheres and less frequently in the brainstem or spinal cord. Glioblastoma is composed of a heterogeneous collection of cancer cells. Unless extremely rare circumstances, it does not spread outside of the central nervous system structures, so it remains circumscribed to the cerebral tissue like in other brain tumours. Moreover, GBM has a dramatic invasive potential and resistance to common therapies: even when treated with the standard therapy (i.e. the *Stupp protocol* [52]-[53]), the median patient survival does not exceed 10-16 months [32] and the five-years survival rate is about 5% ([28]-[44]). Besides the common hallmarks of cancer, glioblastoma shows a peculiar growth along white matter fibres or along vessels, following physical structures in the brain's extracellular environment, making it impenetrable to many conventional drugs. For the same reasons, GBM tends to show three-dimensional irregular spreading patterns [33].

Glioblastoma usually arises as:

- a primary tumour: i.e. the carcinogenesis starts *de novo* and thus, it is not the evolution of lower-grade neoplasms;

Glioma type	Name	Grade	Incidence
Astrocytic	Pilocytic astrocytoma	I	5-6%
	Subependymal gian cell astrocytoma	I	<1%
	Diffusely infiltrating astrocytoma	II	10-15%
	Anaplastic Astrocytoma	III	10-15%
	Glioblastoma multiforme	IV	12-15%
Oligodendroglial	Oligodendroglioma	II	2.5%
	Anaplastic oligodendroglioma	III	1.2%
Oligoastrocytic	Oligoastrocytoma	II	1.8%
	Anaplastic oligoastrocytoma	III	1%
Ependymal	Subependymoma	I	0.7%
	Myxopapillary ependymoma	I	0.3%
	Ependymoma	II	4.7%
	Anaplastic ependymoma	III	1%

Table 1.1: Classification of gliomas according to WHO classification of tumours of the central nervous system [51].

- a secondary tumour: it takes place from the progression of lower-grade neoplasms, in particular as an aggravation of Fibrillary astrocytoma (grade II) and Anaplastic astrocytoma (grade III).

Although GBM is very rare (incidence rate is 3.2 per 100,000 population [23]), it is particularly aggressive and fast. Indeed, it has a rapid progression of 2–3 months [49]. During this period, the 10 most prevalent symptoms (with their incidence rate) are:

- seizures (37%);
- cognitive deficits (36%);
- drowsiness (35%);
- dysphagia (30%);
- headache (27%);
- confusion (27%);
- aphasia (24%);

- motor deficits (21%);
- fatigue (20%);
- dyspnea (20%).

1.2.3. Therapy

The currently approved treatment schedule is known as *Stupp protocol*. It entails a (partial) surgical excision of the tumour. The removed tumour mass is only partially removed to avoid damage to the brain structures. In order to facilitate the surgery, the excision is made following radiotherapy and chemotherapy.

Radiotherapy is a therapy utilizing ionizing radiation administered as part of cancer treatment to control or eliminate malignant cells. Radiation therapy may be curative for certain types of cancer if they are confined to one location of the body.

Chemotherapy, instead, is a pharmacological treatment that kills rapidly dividing cells using strong chemicals. Chemotherapy is most often used to treat cancer because cancer cells grow and divide considerably more rapidly than healthy cells.

Surgery

Choosing the right surgical technique is crucial in order to remove as much tumour mass as possible. Indeed, only a total excision of the tumour (greater than 98% of the tumour mass volume) appears to confer some survival advantages [24]. GBM invariably recurs despite surgical intervention. The protocol usually involves a second intervention in order to reduce the probability of the tumour mass proliferating again in the brain parenchyma.

The healing process is significantly more difficult for recurrences than for first manifestations, but the suggested therapy improves the quality of life and life expectancy.

Radiotherapy

The goal of radiotherapy, which is typically administered after surgery, is to damage the DNA of any tumour cells that have persisted after the operation because they infiltrate the region around the tumour mass. For this reason, it is directed at the part of the brain affected by the operation and a slight external margin. The patient's likelihood of survival rises if radiation is successful in killing these cells before they can fix their DNA and start growing again. The therapy procedure is broken down into numerous daily sessions with various radiation dosages, depending on the age of the patient.

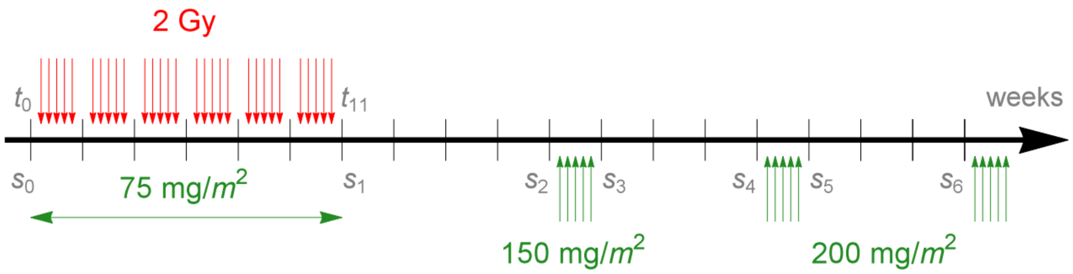

Figure 1.4: The standard Stupp protocol: radiotherapy is administrated at 2 Gy/day five days per week, for six weeks; concomitant chemotherapy with temozolomide at a daily dose of 75 mg/m^2 from beginning until ending of radiotherapy; six cycles of adjuvant chemotherapy at a dose of 150 mg/m^2 (only first cycle) and 200 mg/m^2 (remaining cycles). Image adapted from [45].

Chemotherapy

Chemotherapy is combined with radiation to force tumour cells that have evaded radiotherapy into apoptosis by disrupting DNA organization. The addition of chemotherapy, however, appears to offer glioblastoma patients just a modest benefit (at least in terms of median survival). Although the use of nitrosoureas (anti-cancer medications, e.g. *temozolomide*) did not significantly extend median life in all patients, some individuals appeared to benefit from longer survival when chemotherapy was added.

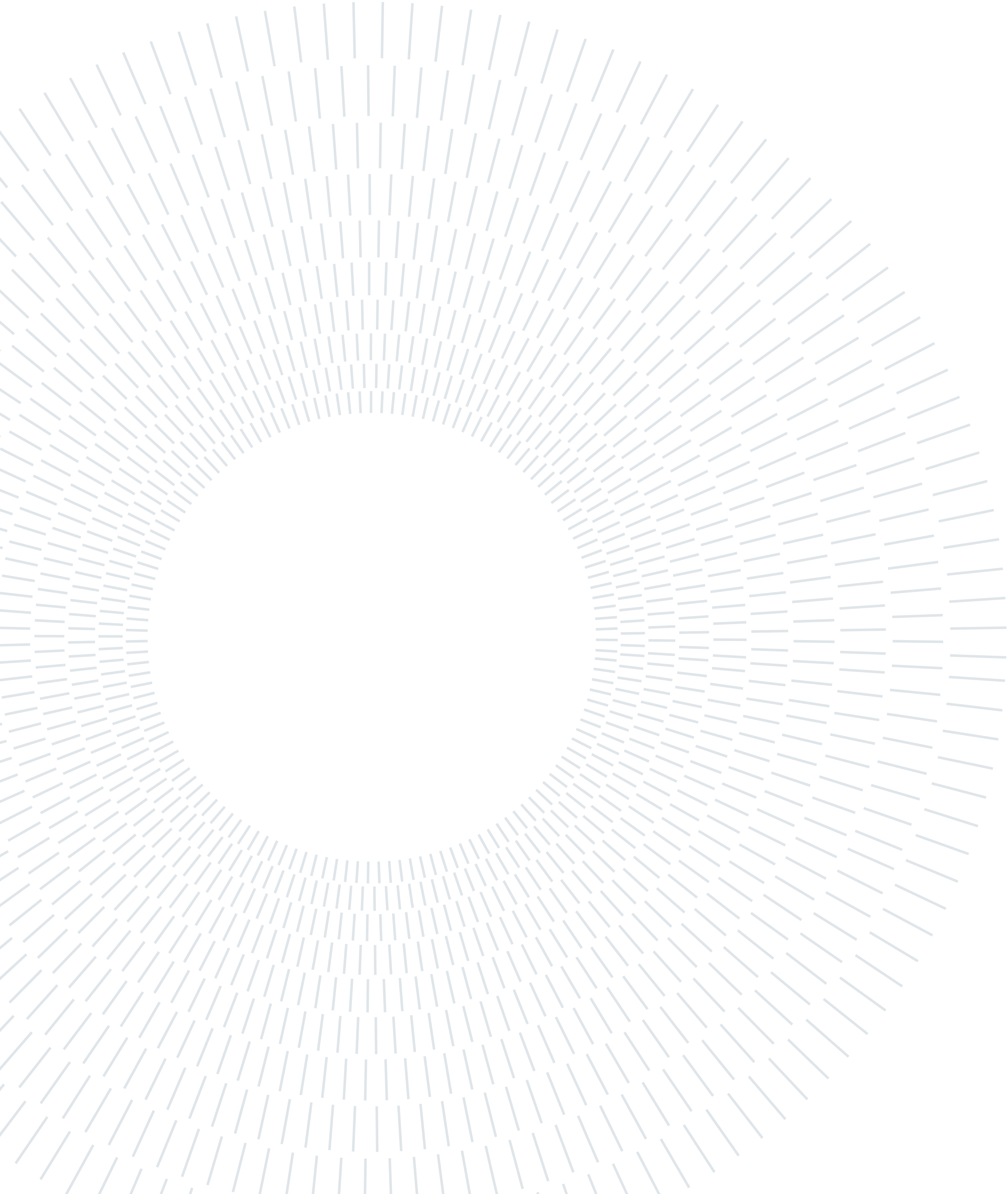

2 | Imaging Techniques

In order to construct patient-specific predictions of GBM growth, we need to reconstruct the computational domain starting from medical imaging techniques. In this Chapter, we provide an overview of the two primary imaging methods for reconstructing brain tumour morphology: Diffusion Tensor Imaging (DTI) and Magnetic Resonance Imaging (MRI). These methods start from medical pictures to give a computational reconstruction of the brain, aiding in the creation of a realistic geometry and taking into account the anisotropy of the brain tissue. Without getting into technical details, which are outside the scope of this work, we summarize the operating principles of MRI and DTI in the chapter to help the reader to have insight into the main steps involved. For more information on these techniques, we refer to [43] and [37].

2.1. Magnetic Resonance Imaging

Magnetic Resonance Imaging, also known as Magnetic Resonance Tomography (MRT) is a technique that allows the reconstruction of detailed body images by exploiting the physical principle of nuclear magnetic resonance. Indeed, it consists of immersing the patient in a static magnetic field $\mathbf{B}_0$ and mapping the response of hydrogen nuclei which create a signal that is processed to form an image of the body in terms of the density of those nuclei in a specific region. Its safety and ability to reproduce images with big contrast and high resolution in all spatial directions, make MRI advantageous with respect to X-rays (which exploit ionizing radiation).

From a physical point of view, it happens that the spins of the protons situated in the magnetic field tend to align with it. Nevertheless, since protons contain an intrinsic magnetic dipole moment due to their spin, the combination of the external field and spin results in a precession around the direction $\mathbf{B}_0$ (as shown in Fig. 2.1). Indeed, a charge in motion produce a magnetic moment μ which combined with the provided static magnetic field $\mathbf{B}_0$ generates a mechanical moment $\mathbf{M} = \mu \times \mathbf{B}_0$ Precession occurs according to an angular frequency known as the Larmor frequency ω.

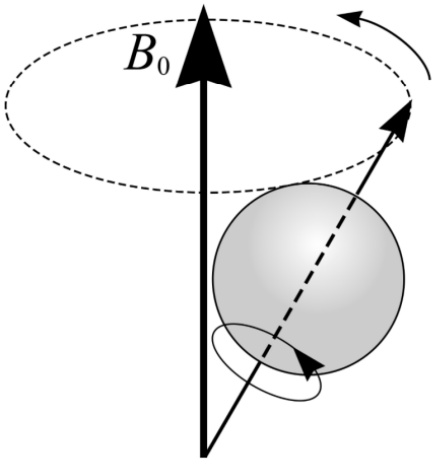

Figure 2.1: Representation of the precession motion of an atom identified as a sphere around the direction of the external magnetic field $\mathbf{B}_0$ [5].

When the applied magnetic field is sufficiently strong, the magnetic dipoles of the protons tend to align with it in orientations that depend on the energy of the nuclei, since the spin-up and spin-down verses reflect two distinct energy situations, at low and high energies, respectively. Because of its high energy consumption, the spin-down state occurs less frequently than the other. This results in macroscopic magnetization based on the direction and polarity of the magnetic field itself.

The magnetic field is then disturbed by a radio-frequency impulse, i.e. a fluctuating magnetic field wave with the same Larmor frequency so that the resonance condition can occur. This results in a drop in longitudinal magnetization and a rise in transverse magnetization, which is no longer null. If the pulse is turned off, the protons will eventually revert to their original state, with the longitudinal magnetization returning to its maximum value and the transverse magnetism disappearing. Such a recovery of the original state, with null magnetization $\mathbf{M}$, is hypothesized to occur exponentially and be regulated by two defining time constants [37]:

$$M_z(t) = M_0(1 - e^{-t/T_1}) \tag{2.1}$$

$$M_x(t) = M_0 e^{-t/T_2} \tag{2.2}$$

where M_z denotes the magnitude of the longitudinal magnetization, M_x is the magnitude of the transverse magnetization, T_1 is the *longitudinal relaxation time* and represents the characteristic time for the quantity M_z to rise up from 0 to M_0. Finally, T_2 is the *transverse relaxation time* and is proportional to the time needed to fall down to 0 from

M_0 (fig. 2.2).

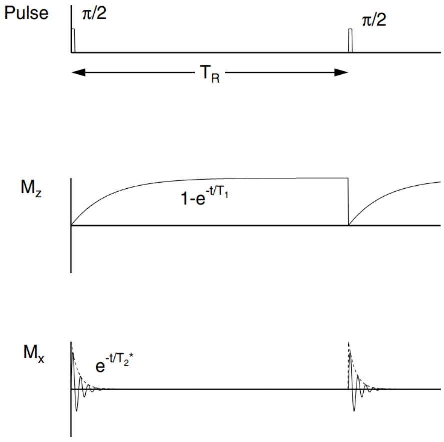

Figure 2.2: Pulse sequence and signal for a free-induction-decay measurement for the components M_z and M_x of $\mathbf{M}$ [37].

From a chemical viewpoint, T_1 and T_2 are both related to the freedom of motion of molecules. In particular, T_1 has bigger values for water and other aqueous substances (due to the low interaction between molecules) as well as for solid structures (since stiff inter-molecular connections impede their energetic interaction). Meanwhile, it is smaller for solutions and parenchyma (in relation to the amount of water contained) and for adipose tissues. T_2 shows the opposite behaviour being lower for former cases and greater for the latter. The resulting image of this technique exploiting the increasing phase and the decreasing phase is shown in Fig. 3.1.

2.2. Diffusion Tenosor Imaging

Diffusion Tensor Imaging (DTI) is a technique that exploits the diffusivity of water molecules in the three spatial directions to measure anisotropies in the distribution of nutrient and tumour diffusion within each voxel of the image, i.e. each volume element. This approach reveals variations in the thermal diffusive motion of protons (of water molecules) in a biological tissue; the more dramatic these variations are, the clearer the area of interest appears. This allows us to map the orientations of the brain fibres, which are bundles of axons that connect cortical areas within the same cerebral hemisphere. In this respect, DTI is employed to evaluate the integrity of the white matter, specifically to investigate possible demyelinating disorders (such as multiple sclerosis), degenerative diseases (such as Alzheimer's disease), and brain cancers that invade fibre bundles.

After detailing the mathematical model in the next chapters, we will perform simulations

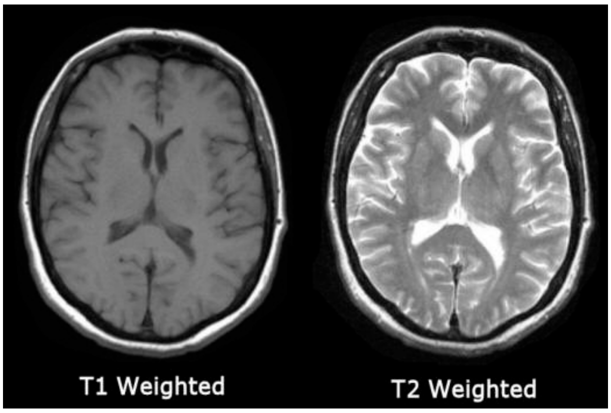

Figure 2.3: Comparison between a T_1-weighted and a T_2-weighted MRI brain imaging. In the T_1 image, grey matter appears dark, whilst the cerebrospinal fluid is the darkest and white matter is the brightest. Conversely, in the T_2 image, the grey matter is brighter than white matter, while the fluid is the brightest [8].

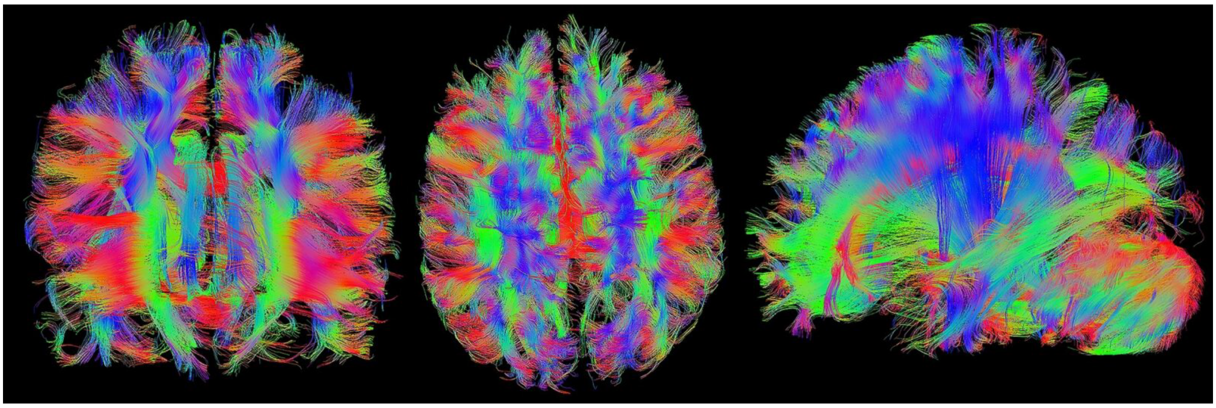

Figure 2.4: Brain images acquired in magnetic resonance imaging with DTI. From left to right: find the coronal section, axial section and sagittal section [7].

on a brain geometry that was created from MRI and DTI data. Thanks to these techniques it is even possible to point-wise define the diffusion tensor D and the preferred direction tensor T which respectively describe the diffusion of the nutrient (oxygen) in the spatial direction and the preferential motility of the tumour.

3 | A diffuse interface model of GBM growth

In this Chapter, we introduce a mathematical model which describes the morphological development of a solid tumour. In contrast to liquid tumours, which are constituted of cancerous cells in suspension in body fluids, solid tumours are a compact mass of tissue that grows preserving the physiological structure of healthy tissue, namely they are composed of the parenchyma and the stroma.

The development of a solid tumour is influenced by several elements. The principal ones are cell-cell and cell-matrix interaction, the mechanical stress stored within the tumour, cell motility, the degree of heterogeneity in cell proliferation, the distribution of nutrients and the rate of consumption. These aspects are highly patient-specific, as shown in [10]. Thus, a mathematical model which describes tumour growth should take into account this variability over patients in order to be as accurate as possible.

Understanding the specificity of a cancerous tumour model parameters for each clinical case may be essential for preventing its spread to surrounding tissue [20]. For these reasons, patient-specific mathematical models of tumour growth are of utmost importance.

In literature, many different approaches to tumour modelling have been developed. The proposed models can be roughly divided into two classes.

- **Sharp interface models**. These models postulate the existence of a zero-thickness interface between the tumour and the healthy tissue. Although this model represents faithfully the physical state having a truly sharp interface, a thin transition region also requires an adaptive grid with elements having a very fine size. Thus, these models usually have a higher computational cost [48].
- **Diffuse interface models**: The interface between the tumour and the surrounding environment is represented by a narrow (but of finite thickness) transition layer. The transition region is in this case modelled as a smoothed function. This approach eliminates the need to enforce complicated boundary conditions across the phases

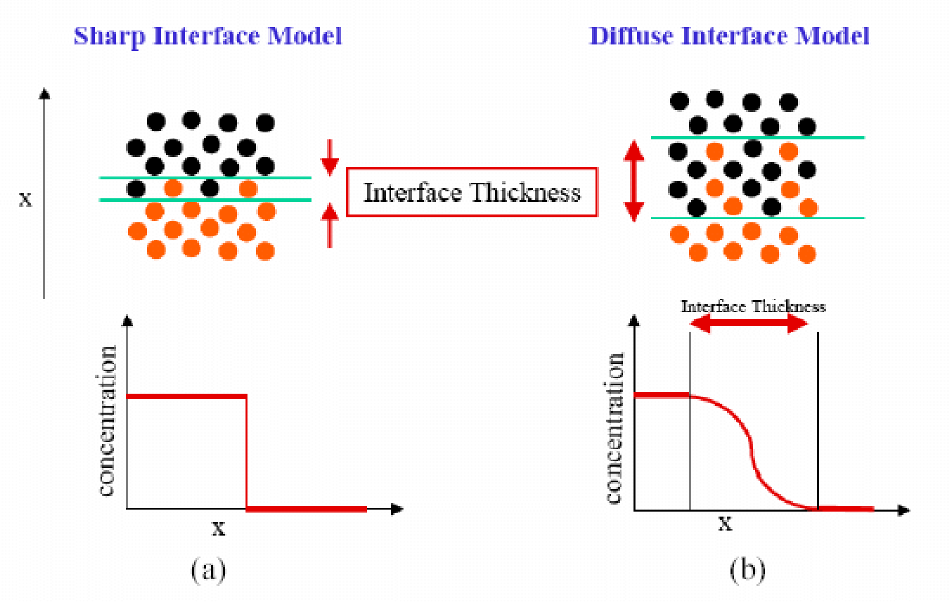

Figure 3.1: Different modellization for the transition between phases at interface layer. On the left (a), is the sharp interface model case. On the right (b), the diffuse interface model case [58].

that would have to be satisfied if the interfaces were assumed sharp. The diffuse interface methodology also has the advantage that there is no need to explicitly track the interface as is required in the sharp interface framework [59].

In this Chapter, we propose a mathematical model based on the second approach. Specifically, the model provided here is a continuous diffuse-interface model based on mixture theory. In the following, we follow the approach described in [12, 29]. For a detailed description of mixture theory, the reader is referred to [13, 26].

3.1. Kinematics of mixture theory

Mixture theory is the application of the methodologies of one-component continuum mechanics to media that are composed of several distinct constituents. The characteristic size of each component of the mixture (in our case, the cells of the brain) is much smaller than the characteristic size of the body under consideration (i.e. the brain). Therefore, it is reasonable to assume that each component can occupy a fraction of each volume element of the system.

The fundamental assumption of this theory is that the space in a mixture may be co-occupied at every location by its components, each of which can be seen as a continuum in its own right.

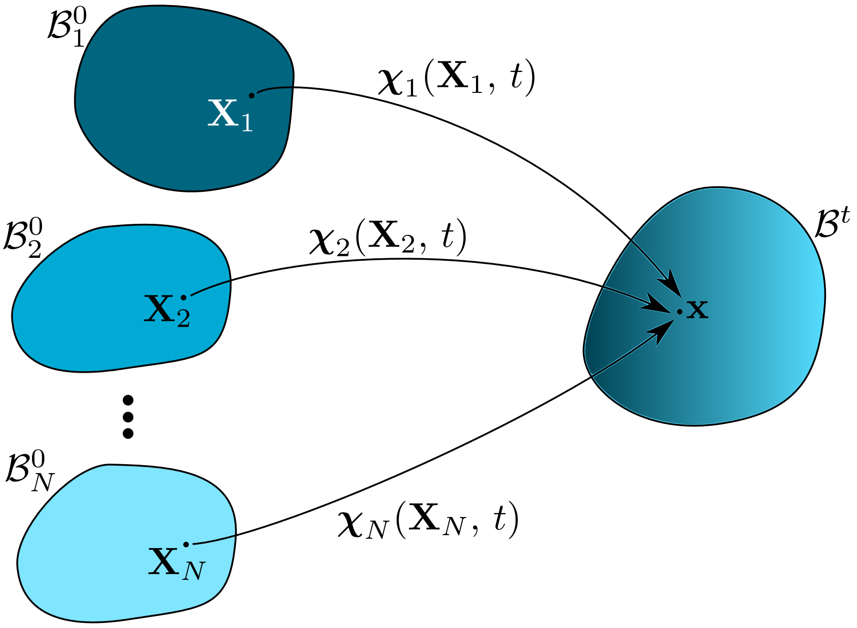

Figure 3.2: The transformations χ_i from the reference configuration $\mathcal{B}_i^0$ to the configuration as a mixture $\mathcal{B}_t$ at a generic time t [41].

In the theory of mixtures, the reference configuration of each i-th constituent is represented as a regular subset $\mathcal{B}_i^0$ of (material) points $\mathbf{X}_i$ (fig.3.2). Each material point is assumed to be composed of at least one of the N constituents, in the following called *phases*, which can be either liquids or solids.

The actual placement of the material point $\mathbf{X}_i$ at a specific time t is described by the function $\boldsymbol{\chi}_i : \mathcal{B}_i^0 \times [t_0, t_1] \to \mathbb{R}^3$. We denote by $\mathbf{x}$ the actual position at time t of the point $\mathbf{X}_i$, that can contains material from all constituents, i.e.

$$\mathbf{x} = \boldsymbol{\chi}_i(\mathbf{X}_i, t). \tag{3.1}$$

Let $\mathcal{B}_i^t$ be the actual configuration at time t of the body, so that

$$\mathcal{B}_i^t = \boldsymbol{\chi}_i(\mathcal{B}_i^0, t).$$

Tue union of all these points gives us the actual configuration of the whole mixture that over time is pointed as $\mathcal{B}^t = \cup_i \mathcal{B}_i^t$.

In particular, the function $\boldsymbol{\chi}_i(\cdot, t)$, where t is a given instant of time, is assumed to be invertible, so that

$$\mathbf{X}_i = \boldsymbol{\chi}_i^{-1}(\mathbf{x}, t). \tag{3.2}$$

From this, one can straightforwardly define the Eulerian velocity at time t of the i-th constituent as

$$\mathbf{v}_i(\mathbf{x},t) = \left.\frac{\partial \boldsymbol{\chi}_i(\mathbf{X}_i,t)}{\partial t}\right|_{\boldsymbol{\chi}_i^{-1}(\mathbf{x},t)} \tag{3.3}$$

We now consider a generic scalar function $\psi(\mathbf{x},t)$ it is possible to express its material (or Lagrangian) derivative as:

$$\dot{\psi} = \frac{d\psi(\mathbf{x},t)}{dt} = \frac{\partial \psi(\mathbf{x},t)}{\partial t} + \mathbf{v}(\mathbf{x},t)\cdot\nabla_x\psi(\mathbf{x},t) \tag{3.4}$$

Where ∇_x is the spatial gradient.

Moreover, it is useful to define a mean value among the velocity of each constituent weighted on their concentration, the *average velocity* of the mixture:

$$\mathbf{v} = \sum_{i=1}^{N} \phi_i \mathbf{v}_i \tag{3.5}$$

We now take a spherical neighbourhood centred in $\mathbf{x}$, indicated as

$$\mathcal{U}_\varepsilon(\mathbf{x}) = \left\{x_\varepsilon \in \mathbb{R}^3 \,\text{s.t.}\, \|\mathbf{x} - \mathbf{x}_\varepsilon\| < \varepsilon\right\}.$$

Given a subset $\mathcal{P} \subseteq \mathcal{B}^t$, we indicate its volume by $V(\mathcal{P})$. The set $\mathcal{P}$ can contain different constituents. For each of them, we indicate the mass of the i^{th} constituent contained in the subset $\mathcal{P}$ by $m_i(\mathcal{P},\, t)$. The volume occupied by such a material is denoted by $V_i(\mathcal{P},\, t)$. We remark that $V(\mathcal{P})$ is generally different from $V_i(\mathcal{P},\, t)$.

We are now able to introduce the following quantities:

- the *true mass density*:

$$\gamma_i(\mathbf{x},t) = \lim_{\varepsilon\to 0} \frac{m_i(\mathcal{U}_\varepsilon(\mathbf{x}),\, t)}{V_i(\mathcal{U}_\varepsilon(\mathbf{x}),\, t)}, \tag{3.6}$$

- the *apparent mass density*:

$$\rho_i(\mathbf{x},t) = \lim_{\varepsilon\to 0} \frac{m_i(\mathcal{U}_\varepsilon(\mathbf{x}), t)}{V(\mathcal{U}_\varepsilon(\mathbf{x}))}. \tag{3.7}$$

Thereby, we can introduce the *volume fraction* ϕ_i, a quantity that represents the ratio of the volume of the i^{th} phase over the total volume:

$$\phi_i(\mathbf{x},t) = \lim_{\varepsilon\to 0} \frac{V_i(\mathcal{U}_\varepsilon(\mathbf{x}), t)}{V(\mathcal{U}_\varepsilon(\mathbf{x}))} = \frac{\rho_i(\mathbf{x},t)}{\gamma_i(\mathbf{x},t)}. \tag{3.8}$$

Finally, the density of the whole mixture is defined as:

$$\rho(\mathbf{x},t) = \lim_{\varepsilon\to 0} \frac{M(\mathcal{U}_\varepsilon(\mathbf{x}), t)}{V(\mathcal{U}_\varepsilon(\mathbf{x}))} = \lim_{\varepsilon\to 0} \frac{1}{V(\mathcal{U}_\varepsilon(\mathbf{x}))} \sum_{i=1}^{N} m_i(\mathcal{U}_\varepsilon(\mathbf{x}), t) = \sum_{i=1}^{N} \rho_i(\mathbf{x}, t), \tag{3.9}$$

where $M(\mathcal{P}, t)$ is the mass of the mixture in $\mathcal{P}$ at time t. Under the hypothesis of full saturation, i.e. each point of the control volume is fully occupied by the N constituents, we have

$$\sum_{a=1}^{N} V_i(\mathcal{U}_\varepsilon(\mathbf{x}), t) = V(\mathcal{U}_\varepsilon(\mathbf{x})) \implies \sum_{a=1}^{N} \phi_i(\mathbf{x},t) = 1 \quad \forall \mathbf{x} \in \mathcal{B}_t \quad \forall t \in [t_0, t_1]. \tag{3.10}$$

We now introduce the continuity equations. For each constituent we enforce that, in each subset $\mathcal{B}_t^* \in \mathcal{B}_t$ with volume V_t^*, the variation of total mass equals the production/consumption of the source term, namely

$$\frac{d}{dt}\int_{\mathcal{B}_t^*} \rho_i d\mathcal{B} = \int_{\mathcal{B}_t^*} \Gamma_i d\mathcal{B} \quad \forall i = 1, ..., N \tag{3.11}$$

where $\Gamma_i(\mathbf{x},t)$ is the mass source term per unit volume.

Now, we can exploit sequentially *Reynold's theorem* and *divergence theorem* to obtain

$$\frac{d}{dt}\int_{\mathcal{B}_t^*} \rho_i d\mathcal{B} = \int_{\mathcal{B}_t^*} \frac{\partial \rho_i}{\partial t} d\mathcal{B} + \oint_{\partial\mathcal{B}_t^*} \rho_i \mathbf{v}_i \cdot \mathbf{n}\, dS = \int_{\mathcal{B}_t^*} \left\{ \frac{\partial \rho_i}{\partial t} + \nabla \cdot (\rho_i \mathbf{v}_i) \right\} d\mathcal{B} \quad \forall i = 1, ..., N \tag{3.12}$$

Where $\mathbf{n}$ is the outward normal versor of the surface element dS. Since the control volume $\mathcal{B}_t^*$ is arbitrary, the continuity equations can be cast in local form. Indeed, from Eq. (3.12) we get

$$\frac{\partial \rho_i}{\partial t} + \nabla \cdot (\rho_i \mathbf{v}_i) = \Gamma_i \quad \forall i = 1, ..., N \tag{3.13}$$

Dividing by the true mass density $\gamma_i(\mathbf{x},t)$, we obtain:

$$\frac{\partial \phi_i}{\partial t} + \nabla \cdot (\phi_i \mathbf{v}_i) = \frac{\Gamma_i}{\gamma_i} \quad \text{a.e.} \forall i = 1, ..., N \tag{3.14}$$

that describes the evolution over time of the volume fraction of the phase i over time.

3.2. Solid tumours as biphasic mixtures

We now specialize in the setting of mixture theory to model the GBM growth. We assume that the brain is a mixture composed of a cellular phase with volume fraction $\phi_c(\mathbf{x}, t)$ representing the tumour and a liquid phase with volume fraction $\phi_l(\mathbf{x}, t)$ which represents the health host tissue (similarly to the model proposed in [46]). Under these conditions, the saturation constraint (3.10) simplifies into

$$\phi_c(\mathbf{x},\, t) + \phi_l(\mathbf{x},\, t) = 1. \tag{3.15}$$

We also assume that the two phases have a density roughly equal to the one of water γ. As we have seen in the previous section, the following form of the mass balance holds true:

$$\frac{\partial \phi_i}{\partial t} + \nabla \cdot (\phi_i \mathbf{v}_i) = \frac{\Gamma_i}{\gamma} \quad i \in \{c, l\} \tag{3.16}$$

To enforce the incompressibility of the whole mixture, we prescribe that $\Gamma_c = -\Gamma_l$. Indeed, if we sum the two continuity equations in (3.16), we obtain

$$\nabla \cdot (\phi_c \mathbf{v}_c + \phi_l \mathbf{v}_l) = \nabla \cdot \mathbf{v} = 0 \tag{3.17}$$

where we have used the saturation constraint (3.15) and $\mathbf{v}$ is the average velocity of the mixture defined in (3.5).

We introduce the scalar field ϕ, defined as the difference between the volume fractions

$$\phi = \phi_c - \phi_l. \tag{3.18}$$

By subtracting the two coninuity equations (3.16)

$$\frac{\partial (\phi_i - \phi_c)}{\partial t} + \nabla \cdot (\phi_i \mathbf{v}_i - \phi_c \mathbf{v}_c) = \frac{\Gamma_i - \Gamma_c}{\gamma} \tag{3.19}$$

Let $\mathcal{J}_c$ and $\mathcal{J}_l$ be the mass fluxes of the two phases with respect to the mixture velocity $\mathbf{v}$

$$\mathcal{J}_c = \gamma \phi_c (\mathbf{v}_c - \mathbf{v}), \tag{3.20}$$

$$\mathcal{J}_l = \gamma \phi_l (\mathbf{v}_l - \mathbf{v}). \tag{3.21}$$

By introducing $\mathcal{J} = \frac{1}{\gamma}(\mathcal{J}_c - \mathcal{J}_l)$ and subtracting Eqs. (3.20)-(3.21), we get

$$\phi_c \mathbf{v}_c - \phi_l \mathbf{v}_l = \phi \mathbf{v} + \mathcal{J}. \tag{3.22}$$

We can use Eq. (3.22) to rewrite Eq. (3.19) as follows

$$\frac{\partial \phi}{\partial t} + \nabla \cdot (\phi \mathbf{v}) + \nabla \cdot \mathcal{J} = \frac{\Gamma}{\gamma} \quad \text{with} \quad \Gamma = \Gamma_c - \Gamma_l. \tag{3.23}$$

We assume that the mixture is very viscous. Furthermore, the mixture is free of external forces. We use a diffuse interface technique to determine a thermodynamically consistent formulation for the mass flux. We take the following definition of Helmholtz free energy:

$$F(\phi) = \int_{\mathcal{B}_t} \left(\kappa \Psi(\phi) + \frac{\epsilon^2}{2} |\nabla \phi|^2 \right) d\mathcal{B}_t, \tag{3.24}$$

where $\mathcal{B}_t$, the region occupied by the brain is assumed to be with fixed boundaries over time. From now on we omit the time specification and we refer to the domain with the symbol $\mathcal{B}$. The two addends represent the intra-phase energy density and the interface energy arising from the interaction between the two different phases, respectively [9].

In this specific case, we take as cell-cell interaction potential $\Psi(\phi)$ a function with a double-well shape, such that its minima are attained in $\phi = 1$ and $\phi = -1$, corresponding to the two pure phases. A simple admissible choice is given by

$$\Psi(\phi) = \frac{1}{4}(1 - \phi^2)^2. \tag{3.25}$$

Fick's first law assumes that diffusion is proportional to the concentration gradient: the flux flows from regions of high concentration to regions of low concentration, with a magnitude proportional to the concentration gradient (spatial derivative). In simpler terms, Fick's law prescribes that a solute moves from a region of higher concentration to a region of lower concentration across a concentration gradient [54].

We can exploit this law to postulate $\mathcal{J}$ to be proportional to the gradient of a chemical potential $\mu = \frac{\delta F(\phi)}{\delta \phi}$, where δ is the *Gâteaux functional derivative.*

Definition 3.2.1 (Gâteaux derivative)**.** Let X and Y be normed spaces, let U be an open subset of X, let $f : U \to Y$ be a function, and let $x_0 \in U$. If there is some $T \in \mathscr{B}(X, Y)$, where $\mathscr{B}(X,Y)$ is a linear map, such that for all $v \in X$ we have

$$\lim_{t \to 0} \frac{f\left(x_0+tv\right)-f\left(x_0\right)}{t} = Tv \tag{3.26}$$

then we say that f is Gâteaux differentiable at x_0 and call T the Gâteaux derivative of f at x_0 [15].

Thus, we assume that

$$\mathcal{J} = -\frac{1}{M_0}\mathsf{T}\nabla\mu \tag{3.27}$$

where M_0 is a friction coefficient. T here represent the preferential motility tensor, which, as said in Section 2.2, takes into account for the anisotropy in the growth of the tumour that prefers to move along brain fibres.

To close the model, we prescribe that Γ depends on the local oxygen concentration by setting

$$\Gamma = \Gamma(\phi, n) = \nu\gamma\Big(\frac{n}{n_s} - \delta\Big)h(\phi). \tag{3.28}$$

Here, ν is the tumour cells proliferation rate, n represents the local concentration of the oxygen, n_s is a physiological value for oxygen concentration in brain tissue , δ is the hypoxia threshold, and $h(\phi)$ is a function that allows the proliferation in the natural range of ϕ.

The function h should be constitutively prescribed. It should turn off tumour cell proliferation when $\phi = -1$, i.e. when we are in the correspondence of the absence of the tumour. A possible choice for h is given by

$$h(\phi) = \max(\min(1, \frac{1}{2}(1+\phi)), 0) \tag{3.29}$$

The dynamic of oxygen concentration is modelled by means of a reaction-diffusion equation. Indeed, we prescribe for the variable n the following evolution in time

$$\frac{\partial n}{\partial t} = \nabla \cdot (\mathsf{D}\nabla n) + S_n\left(1 - \frac{n}{n_s}\right)\frac{n_s}{3}(2-\phi) - \delta_n n h(\phi), \tag{3.30}$$

where D is the diffusivity tensor of the nutrient, S_n is the *oxygen supply rate* and δ_n is the *oxygen consumption rate.*

To sum up, we now present the complete closed system of partial differential equations:

$$\begin{cases} \dfrac{\partial \phi}{\partial t} = \nabla \cdot \left(\dfrac{1}{M_0} \mathsf{T} \nabla \mu \right) + \nu (n - \delta) h(\phi), & (3.31a) \\ \mu = \kappa \Psi'(\phi) - \epsilon^2 \Delta \phi, & (3.31b) \\ \dfrac{\partial n}{\partial t} = \nabla \cdot (\mathsf{D} \nabla n) + S_n \left(1 - \dfrac{n}{n_s} \right) \dfrac{n_s}{3} (2 - \phi) - \delta_n n h(\phi). & (3.31c) \end{cases}$$

Here, we introduce T, the tensor of preferential mobility, which embodies the spatial anisotropy in the tumour growth.

3.3. Boundary and initial condition

It now remains to define the boundary and initial conditions used in the simulations before moving on to the nondimensionalization of the model. Specifically, as an initial condition on $\phi_0(\mathbf{x}) = \phi(\mathbf{x}, 0)$ we chose an exponential distribution in space centred at the centre of gravity of the region occupied by the tumour during the growth $\mathbf{x_0}$. From this, we retrieve $\mu_0(\mathbf{x}) = \mu(\mathbf{x}, 0)$ computing the operators on ϕ_0 and $n_0(\mathbf{x}) = n(\mathbf{x}, 0)$ by simply solving the stationary version of the nutrient equation:

$$\phi_0 = 2e^{-\alpha_0 \|\mathbf{x} - \mathbf{x_0}\|^4} - 1 \quad \text{in } \mathcal{B}, \qquad (3.32a)$$

$$\mu_0 = \kappa \Psi'(\phi_0) - \epsilon^2 \Delta \phi_0 \quad \text{in } \mathcal{B}, \qquad (3.32b)$$

$$0 = \nabla \cdot (\mathsf{D} \nabla n_0) + S_n \left(1 - \frac{n_0}{n_s} \right) \frac{n_s}{3} (2 - \phi) - \delta_n n_0 h(\phi) \quad \text{in } \mathcal{B}. \qquad (3.32c)$$

Since both tumour and nutrient cannot diffuse beyond the skull , we impose the homogeneous Neumann on the boundary $\partial\mathcal{B}$ for all three variables considered:

$$\nabla \phi \cdot \mathbf{n} = 0 \quad \text{on } \partial\mathcal{B}, \qquad (3.33a)$$

$$\nabla \mu \cdot \mathbf{n} = 0 \quad \text{on } \partial\mathcal{B}, \qquad (3.33b)$$

$$\nabla n \cdot \mathbf{n} = 0 \quad \text{on } \partial\mathcal{B}, \qquad (3.33c)$$

where $\mathbf{n}$ is the outward normal vector.

3.4. Nondimensionalization

It is useful to derive the nondimensionalized form of the system of equation (3.31). To pursue this aim, we adopt as characteristic quantities L_{car}, T_{car} and ϵ_{car}, respectively *characteristic length*, *characteristic time* and *characteristic diffuse interface thickness* . If the first two are fixed for an obvious reason since the growth model relies on spatial and temporal features, the latter is chosen for its dependency on the mesh. For the nondimensionalization we set the following characteristic quantities:

- $T_{\text{car}} = 0.5\,\text{day}$
- $L_{\text{car}} = 10\,\text{mm}$
- $\epsilon_{\text{car}} = 30\,\text{Pa}^{1/2}\text{mm}$

In such a way, we obtain the following nondimensional quantities:

- $\hat{\mu} = \frac{L_{\text{car}}^2}{\epsilon_{\text{car}}^2}\mu$
- $\hat{n} = \frac{1}{n_s}n$
- $\hat{\nu} = T_{\text{car}}\nu$
- $\hat{M}_0 = \frac{L_{\text{car}}^4}{\epsilon_{\text{car}}^2 T_{\text{car}}}M_0$
- $\hat{\epsilon} = \frac{1}{\epsilon_{\text{car}}}\epsilon = 1$
- $\hat{k} = \frac{L_{\text{car}}^2}{\epsilon_{\text{car}}^2}k$
- $\hat{\delta} = \delta$
- $\hat{\delta_n} = T_{\text{car}}\delta_n$
- $\hat{S_n} = T_{\text{car}}S_n$
- $\hat{\mathsf{D}} = \frac{T_{\text{car}}}{L_{\text{car}}^2}\mathsf{D}$

Given that, the system (3.31) is written in the nondimensionalized variables as follows:

$$\begin{cases} \dfrac{\partial\hat{\phi}}{\partial t} = \nabla \cdot \left(\dfrac{1}{\hat{M}_0}\mathsf{T}\nabla\hat{\mu}\right) + \nu(\hat{n} - \delta)h(\phi), & (3.34a) \\ \hat{\mu} = \hat{\kappa}\Psi'(\phi) - \Delta\phi, & (3.34b) \\ \dfrac{\partial\hat{n}}{\partial t} = \nabla \cdot (\mathsf{D}\nabla\hat{n}) + S_n\left(1 - \hat{n}\right)\dfrac{1}{3}(2 - \phi) - \delta_n\hat{n}h(\phi). & (3.34c) \end{cases}$$

For the sake of simplicity, from now on we can omit the hat symbol.

3.5. Biological parameters

The selection and calibration of equations parameters are crucial steps to have realistic simulations. The identification of patient-specific parameters is a key step to transferring

	Parameter description	Range of values	Ref.
M_0	Tumour inter-phase friction	$1377.86 - 5032.2$ (Pa day) /mm^2	Swabb et al [56]
ν	Tumour cells proliferation rate	$0.012 - 0.5$ day $^{-1}$	Swanson et al [57] and Martinez-Gonzalez et al [40]
S_n	Oxygen supply rate	$10^3 - 10^5$ day $^{-1}$	Chatelain et al [18]
δ_n	Oxygen consumption rate	$10^3 - 10^5$ day $^{-1}$	Martinez-Gonzalez et al [40]
κ	Brain Young modulus	$106.66 - 1533.3$ Pa	Clatz et al [19]
δ	Hypoxia threshold	$0.1 - 0.33$	Bedogni and Powell [14]

Table 3.1: Biological range found in literature for the parameters of the model.

the mathematical model proposed in this thesis to clinical settings. Here, parameters are chosen in a range compatible with current measurements that we have found in the literature, as reported in Table 3.1. Accordingly, we identify a set of admissible non-dimensional parameters $\mathcal{P} = [\nu, M_0, \kappa, \delta, \delta_n, S_n]$:

$$\begin{aligned}\mathcal{P}_{\text{bio}} = \{&[0.1, 0.4], [2000.0, 4000.0], [600.0, 900.0], [0.2, 0.3],\\ &[5000.0, 50000.0], [5000.0, 50000.0]\}\end{aligned}$$

3.6. Numerical framework

In this section, we describe the discretization approach used to numerically solve the system (3.34). The mesh of the brain is acquired via the techniques described in Ch.2. The domain is partitioned in tetrahedral elements. We refer to this partition as $\mathcal{T}_h$. Then, we divide the temporal interval [0,T] into N discrete sub-intervals $\Delta t = T/N$. The n-th simulation time-point $t^n = n\Delta t$ with $n = 0, ..., N$. Next, we introduce the finite element space $V_h = \left\{\chi \in C^0(\Omega) : \chi|_{K_j} \in \mathbb{P}^1(K_j) \quad \forall K_j \in \mathcal{T}_h\right\} \subset H^1(\Omega)$, which is the space of continuous functions that are polynomial of grade 1 ($\mathbb{P}^1$) when restricted on the element K_j. V_h is a subset of the Hilbert space $H^1(\Omega)$ that contains $L^2(\Omega)$ functions whose first weak derivative is in $L^2(\Omega)$ too.

Thus, given the initial data $(\phi_h^0, n_h^0) \in V_h \times V_h$ we obtain the following discrete problem:

$$\begin{cases}\left(\dfrac{\phi_h^{n+1} - \phi_h^n}{\Delta t}, \varphi_h\right) = -\dfrac{1}{M_0}\left(\mathsf{T}\nabla\mu_h^{n+1}, \nabla\varphi_h\right) + \nu\left(\left(n_h^{n+1} - \delta\right) h\left(\phi_h^n\right), \varphi_h\right) & (3.35a)\\ \left(\mu_h^{n+1}, v_h\right) = \left(\nabla\phi_h^{n+1}, \nabla v_h\right) + \kappa\left(\Psi_c'\left(\phi_h^{n+1}\right), v_h\right) + \kappa\left(\Psi_e'\left(\phi_h^n\right) v_h\right) & (3.35b)\\ \left(\dfrac{n_h^{n+1} - n_h^n}{\Delta t}, q_h\right) = -\left(\mathsf{D}\nabla n_h^{n+1}, \nabla q_h\right) + S_n\left(\left(1 - n_h^{n+1}\right)\dfrac{1}{3}\left(2 - \phi_h^n\right), q_h\right) & (3.35c)\\ \qquad - \delta_n\left(n_h^{n+1} h\left(\phi_h^n\right), q_h\right) & \end{cases}$$

where $(\cdot, \cdot)$ denotes the standard L^2 inner product over Ω . In order to ensure the gradient stability of the scheme, we prescribe the following splitting for the Cahn-Hilliard potential (as suggested in [16]):

- $\Psi_c\left(\phi_h^{n+1}\right) = \frac{\left(\phi_h^{n+1}\right)^4+1}{4}$
- $\Psi_e\left(\phi_h^{n}\right) = -\frac{\left(\phi_h^{n}\right)^2}{2}$

Decomposing the potential in such a way, i.e. in a convex term Ψ_c that we can treat with an implicit scheme and a concave term Ψ_e that is treated with an explicit scheme, ensures the solution to be stable over time [50].

4 | Reduced Order Model

The complexity of the direct problem makes the discrete system 3.35 expensive, from a computational point of view, to be solved. For this reason, in this chapter, we investigate a technique able to reduce the degree of freedom of the problem making the computation of the solution easier. In particular, we apply the *Reduced Basis method* using basis functions calculated by the *Proper Orthogonal Decomposition* (POD). Since the full order model is nonlinear, we bypass the projection of the problem on the reduced space exploiting interpolation through *Neural Networks* (POD-NN) [35].

4.1. Reduced Basis Methods

Reduced basis (RB) methods are computational reduction techniques for the fast and accurate assessment of input-output relationships: the output is written as a functional of the solution of a parametrized partial differential equation (PDE), with the set of parameters serving as the input [47].

An RB approximation aims to capture the key properties of the input/output behaviour of a system by enhancing computing efficiency and by controlling the approximation error between the reduced-order solution and the full-order solution (the parametrized PDE). Particularly, the objective is to approximate a PDE solution with a few degrees of freedom as opposed to the many degrees of freedom required for a full-order approximation.

In fact, the idea behind computational reduction strategies is the assumption (often occurring in real work) that the behaviour of a system may be adequately characterized by a limited number of dominant modes. In this manner, we only need to solve the full-order issue for a small number of instances of the input via a computationally intensive Offline step in order to generate a smaller set of basis solutions.

By describing the reduced solution as a linear combination of the basis solutions and using a Galerkin projection onto this reduced space, it is possible to execute a large number of low-cost reduced-order simulations at a very cheap Online stage for fresh instances of the input.

One of the most popular strategies to construct basis functions and reduced spaces is the Proper Orthogonal Decomposition which reduces the dimensionality of a system by transforming the original variables into a new set of uncorrelated variables (called POD modes, or principal components). The first few modes ideally retain most of the energy present in all of the original variables.

4.2. Proper Orthogonal Decomposition

Starting from the Full Order Model (FOM) described in Ch.3.2 we use proper orthogonal decomposition (POD) reduced-order modelling to obtain a Reduced Order Model (ROM) of the full-order system. This method consists in catching the predominant dynamic of the physical field via some already computed solution, the *snapshots*. Starting from them, it is possible to construct a subspace of reduced dimension through Singular Values Decomposition (SVD) approach. Then, projecting the operators on it, it is possible to compute a solution on this reduced space, simplifying the complexity of the whole problem. We start by calculating the POD basis of a set $\mathcal{P}_k$ of parameters from the snapshots matrices associated with $\theta = \phi, \mu, n$, i.e. the matrices whose columns are the nodal values of the solution at a specific time-step $F_{\theta k} = [f^0_{\theta k}, ..., f^N_{\theta k}]$ for that particular evolution k that comprises N+1 steps. Then applying the following steps, we retrieve a ROM basis $\{\xi^\theta_{kl}\}_{l=1,\dots,N_{\text{POD}}}$:

- prescribe the amount of required information that the POD basis should cover $ic \in (0, 1]$;
- compute the trace $tr(F^t_{\theta k} F_{\theta k})$ of the correlation matrix $F^t_{\theta k} F_{\theta k} = (f^m_{\theta k}, f^l_{\theta k})_{ml} \in M(N+1, \mathbb{R})$, where $(\cdot, \cdot)$ is the chosen inner product;
- set $N^{\text{POD}}_{\theta k} = \min\Big\{m, \Big(\sum_{i\leq m} \lambda_{ki}\Big)/tr(F^t_{\theta k} F_{\theta k}) \leq ic\Big\}$;
- evaluate the pair eigenvalues-eigenvectors $\{\lambda_{ki}, \nu^i_k\}_{i=1,\dots,N^{\text{POD}}_{\theta k}}$ of $F^t_k F_k$;
- set $\xi^\theta_{ks} = \frac{1}{\sqrt{\lambda_{ks}}} \sum_j (\nu^s_k)_j \, f^j_{\theta k}$ where $(1 \leq s \leq N^{\text{POD}}_f)$.

In particular, we start for each parameters set $\mathcal{P}_k$ from a snapshot matrix for each variable: $\mathbf{F}_\phi = [\phi^0_k, ..., \phi^N_k]$, $\mathbf{F}_\mu = [\mu^0_k, ..., \mu^N_k]$ and $\mathbf{F}_n = [n^0_k, ..., n^N_k]$. After computing the eigensystem we choose N^k_{POD} as:

$$N^k_{\text{POD}} = \max\Big\{N^{\text{POD}}_{k\phi}, N^{\text{POD}}_{k\mu}, N^{\text{POD}}_{kn}\Big\} \tag{4.1}$$

To obtain the same dimension for each field, basis is completed with the remaining $N^k_{\text{POD}} -$

$N_{\theta k}^{\mathrm{POD}}$ basis, i.e. $\{\xi_{kl}^{\theta}\}_{l=1,\ldots,N_{\theta k}^{\mathrm{POD}}}$, where $\theta \in \{\phi, \mu, n\}$. We emphasize that POD basis elements are finite element functions.

Now we reason similarly as before but this time we let k vary, in the sense that until this point, we only endowed the ROM basis of parameter-specific information of the evolution over time, but we want a basis able to capture tumour behaviour over the parameters.

In order to build up such a basis, we consider the matrices

$$F_\theta = \left[\xi_{11}^{\theta}, \ldots, \xi_{1N_{\mathrm{POD}}^{1}}^{\theta}, \ldots, \xi_{M1}^{\theta}, \ldots, \xi_{MN_{\mathrm{POD}}^{M}}^{\theta}\right]$$

with $\theta \in \{\phi, \mu, n\}$, where M is the number of parameters sets chosen to build up the basis. We evaluate once again the pair eigenvalues-eigenvectors, this time for the matrix $F_\theta^t F_\theta$ obtaining $\{\lambda_i^\theta, \nu^{\theta i}\}_{i=1,\ldots,N_{\mathrm{POD}}}$ with $\theta \in \{\phi, \mu, n\}$, where N_{POD} is such that the required information contents of the POD bases satisfy $ic = 0.95$; that is, the POD basis contain at least 95.00% of the snapshot information for each variable. Then, for each variable we compute, $\xi_s^\theta = \frac{1}{\sqrt{\lambda_s^\theta}} \sum_j \left(\nu^{\theta s}\right)_j \xi_j^\theta$ where $1 \leq s \leq N_{\mathrm{POD}}^{M}$ and $j = 11, \ldots, MN_{\mathrm{POD}}$.

The final results of the basis construction phase are the following ROM basis $\mathbf{P}_\theta$, $\theta \in \{\phi, \mu, n\}$, that retain most of the information present in all of the original variables:

$$\mathbf{P}_\phi = \left\{\xi_l^\phi\right\}_{l=1,\ldots,N_{\mathrm{POD}}}, \; \mathbf{P}_\mu = \left\{\xi_l^\mu\right\}_{l=1,\ldots,N_{\mathrm{POD}}}, \; \mathbf{P}_n = \left\{\xi_l^n\right\}_{l=1,\ldots,N_{\mathrm{POD}}}.$$

We make now a projection of the variables:

$$\phi_h^n = \sum_{i=1}^{N_{\mathrm{POD}}} \alpha_i^n \xi_i^\phi, \quad \mu_h^n = \sum_{i=1}^{N_{\mathrm{POD}}} \beta_i^n \xi_i^\mu, \quad n_h^n = \sum_{i=1}^{N_{\mathrm{POD}}} \eta_i^n \xi_i^n. \tag{4.2}$$

Substituting Equations 4.6 into Equation 3.35 and choosing $v_h \equiv \xi_m^\phi, w_h \equiv \xi_m^\mu, q_h \equiv \xi_m^n$, we obtain the following ROM system:

$$
\begin{cases}
\begin{aligned}
\sum_{i=1}^{N_{\mathrm{POD}}} \frac{\alpha_i^{n+1}-\alpha_i^n}{\Delta t}\left(\xi_i^\phi,\xi_i^\phi\right) &= -\frac{1}{M_0}\sum_{i=1}^{N_{\mathrm{POD}}} \beta_i^{n+1}\left(\mathsf{T}\nabla\xi_i^\mu,\nabla\xi_i^\phi\right) && \text{(4.3a)}\\
&\quad+\nu\left(\left(\sum_{i=1}^{N_{\mathrm{POD}}}\eta_i^{n+1}\xi_i^n-\delta\right)h\left(\sum_{i=1}^{N_{\mathrm{POD}}}\alpha_i^n\xi_i^\phi\right),\xi_i^\phi\right)\\
\sum_{i=1}^{N_{\mathrm{POD}}} \beta_i^{n+1}\left(\xi_i^\mu,\xi_i^\mu\right) &= \epsilon^2\sum_{i=1}^{N_{\mathrm{POD}}}\alpha_i^{n+1}\left(\nabla\xi_i^\phi,\nabla\xi_i^\mu\right) && \text{(4.3b)}\\
&\quad+\kappa\left(\Psi_c'\left(\sum_{i=1}^{N_{\mathrm{POD}}}\alpha_i^{n+1}\xi_i^\phi\right),\xi_i^\mu\right)\\
&\quad+\kappa\left(\Psi_e'\left(\sum_{i=1}^{N_{\mathrm{POD}}}\alpha_i^{n}\xi_i^\phi\right),\xi_i^\mu\right)\\
\sum_{i=1}^{N_{\mathrm{POD}}} \frac{\eta_i^{n+1}-\eta_i^n}{\Delta t}\left(\xi_i^n,\xi_i^n\right) &= -\sum_{i=1}^{N_{\mathrm{POD}}}\eta_i^{n+1}\left(\mathsf{D}\nabla\xi_i^n,\nabla\xi_i^n\right) && \text{(4.3c)}\\
&\quad+S_n\left(\left(1-\sum_{i=1}^{N_{\mathrm{POD}}}\eta_i^{n+1}\xi_i^n\right)g\left(\sum_{i=1}^{N_{\mathrm{POD}}}\alpha_i^n\xi_i^\phi\right),\xi_i^n\right)\\
&\quad-\delta_n\left(\left(\sum_{i=1}^{N_{\mathrm{POD}}}\eta_i^{n+1}\xi_i^n\right)h\left(\sum_{i=1}^{N_{\mathrm{POD}}}\alpha_i^n\xi_i^\phi\right),\xi_i^n\right)
\end{aligned}
\end{cases}
$$

Where the initial conditions are given by $\alpha_i^0=\left(\phi_h^0,\xi_i^\phi\right)^h$ and $\eta_i^0=\left(\hat{n}_h^0,\xi_i^n\right)^h$. We now replace the steady terms using:

$$
V_{1,ij}:=\left(\xi_i^\phi,\xi_j^\phi\right),\quad U_{1,ij}:=\left(\xi_i^\mu,\xi_j^\mu\right),\quad W_{1,ij}:=\left(\xi_i^n,\xi_j^n\right),
$$

$$
V_{2,ij}:=\left(\mathsf{T}\nabla\xi_i^\mu,\nabla\xi_j^\phi\right),\quad U_{2,ij}:=\left(\xi_i^\phi,\xi_j^\mu\right),\quad W_{2,ij}:=\left(\mathsf{D}\nabla\xi_i^n,\nabla\xi_j^n\right).
$$

In such a way, the system is simplified as follows:

$$
\begin{cases}
\displaystyle\sum_{i=1}^{N_{\text{POD}}} \frac{\alpha_i^{n+1}-\alpha_i^n}{\Delta t} V_{1,ij} = -\frac{1}{M_0}\sum_{i=1}^{N_{\text{POD}}} \beta_i^{n+1} V_{2,ij} & \text{(4.4a)} \\
\displaystyle\qquad + \nu\left(\left(\sum_{i=1}^{N_{\text{POD}}} \eta_i^{n+1}\xi_i^n - \delta\right) h\left(\sum_{i=1}^{N_{\text{POD}}} \alpha_i^n \xi_i^\phi\right), \xi_i^\phi\right) & \\
\displaystyle\sum_{i=1}^{N_{\text{POD}}} \beta_i^{n+1} U_{1,ij} = \epsilon^2 \sum_{i=1}^{N_{\text{POD}}} \alpha_i^{n+1} U_{2,ij} + \kappa\left(\Psi_c'\left(\sum_{i=1}^{N_{\text{POD}}} \alpha_i^{n+1}\xi_i^\phi\right), \xi_i^\mu\right) & \text{(4.4b)} \\
\displaystyle\qquad + \kappa\left(\Psi_e'\left(\sum_{i=1}^{N_{\text{POD}}} \alpha_i^n \xi_i^\phi\right), \xi_i^\mu\right) & \\
\displaystyle\sum_{i=1}^{N_{\text{POD}}} \frac{\eta_i^{n+1}-\eta_i^n}{\Delta t} W_{1,ij} = -\sum_{i=1}^{N_{\text{POD}}} \eta_i^{n+1} W_{2,ij} & \text{(4.4c)} \\
\displaystyle\qquad + S_n\left(\left(1-\sum_{i=1}^{N_{\text{POD}}} \eta_i^{n+1}\xi_i^n\right) g\left(\sum_{i=1}^{N_{\text{POD}}} \alpha_i^n \xi_i^\phi\right), \xi_i^n\right) & \\
\displaystyle\qquad - \delta_n\left(\left(\sum_{i=1}^{N_{\text{POD}}} \eta_i^{n+1}\xi_i^n\right) h\left(\sum_{i=1}^{N_{\text{POD}}} \alpha_i^n \xi_i^\phi\right), \xi_i^n\right) &
\end{cases}
$$

In order to face the non-linearities given in the terms containing the functions Ψ and h, we solve this system of equations via Newton method.

4.3. Surrogate POD with a Neural Network approach

As we have seen in the previous section, the Reduced order model (4.4) is highly nonlinear. The naive application of the reduced basis method required the projection of the matrices representing the model on the reduced space of any new instance of the parameters. For this reason, the computational time of the ROM is similar to or even higher than the one of the FOM. To overcome this issue, in this work, we exploit Neural Networks to directly approximate the mapping of the parameters into the set of ROM coefficients. Using such a data-driven technique (POD-NN) [35], indeed, we are no longer interested in the dynamics of the ROM but just in the value of coefficient over time obtained by projecting the FOM solution onto the reduced space.

Let us consider a generic set of parameters σ. To this set, it corresponds a unique evolution of the FOM. Thus, projecting the solution at each time step t onto the reduced space generated by the reduced basis $\{\xi_l^\theta\}_{l=1,\dots,N_\theta^{\text{POD}}}$, where $\theta \in \{\phi, \mu, n\}$, we obtain a set of coefficient $\{a_l^t\}_{l=1,\dots,N_\theta^{\text{POD}}}$. With this information, it is possible to train a neural network whose results entail a drastic decrease in computational effort.

4.3.1. Neural Networks

Following [35], an artificial neuron represents a simplified model of a biological neuron. Let us consider the neuron j represented on in Fig.4.1a. Suppose that it is connected with m sending neurons $\{s_1, ..., s_m\}$ and n receiving (target) neurons $\{r_1, ..., r_n\}$.

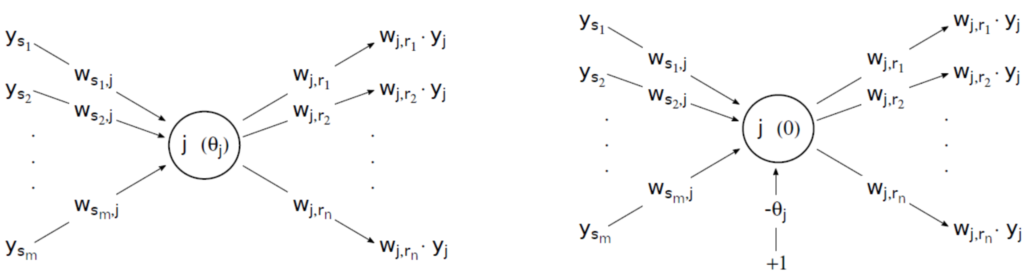

(a) (b)

Figure 4.1: Representation of a generic neuron j of an artificial neural network, including (right) or not (left) a bias neuron. On the left, the neuron accumulates the weighted inputs $\{w_{s_1,j}y_{s_1}, ..., w_{s_m,j}y_{s_m}\}$ respectively coming from the sending neurons $\{s_1, ..., s_m\}$; on the right, the neuron accumulates the weighted inputs $\{w_{s_1,j}y_{s_1}, ..., w_{s_m,j}y_{s_m}, -\theta_j\}$ respectively coming from the sending neurons $\{s_1, ..., s_m, b\}$, with b the bias neuron. In both situations, the neuron then fires y_j, sent to the target neurons $\{r_1, ..., r_n\}$ through the synapsis $\{w_{j,r_1}, ..., w_{j,r_n}\}$. The neuron threshold is reported in brackets within the neuron. [35].

Referring to the output of a generic neuron α at time t with $y_\alpha(t) \in \mathbb{R}$, we weight it with a value $w_{\alpha,\beta}$ when it is connected to the neuron β in the adjacent layer. Notice that time is discretized in the context of *atificial neural networks* (ANNs) by adding the timestep Δt. Clearly, this is not realistic from a biological standpoint; yet, it simplifies the implementation significantly. To simplify the notation, we shall not indicate dependence on time unless it is absolutely required. Three functions fully describe an artificial neuron j: the *propagation function*, the *activation function* and the *output function*. The propagation function f_{prop} collects the vectorial input $\mathbf{p} = [y_{s_1}, ..., y_{s_m}]^T \in \mathbb{R}^m$ into a scalar u_j often called *net input*, i.e.,

$$u_j = f_{\text{prop}}(w_{s_1,j}, ..., w_{s_m,j}, y_{s_1}, ..., y_{s_m}).$$

A common choice is to pick f_{prop} as the weighted sum:

$$f_{\text{prop}}(w_{s_1}, ..., w_{s_m}, y_{s_1}, ..., y_{s_m}) = \sum_{k=1}^{m} w_{s_k,j} y_{s_k}$$

At each timestep, the activation state a_j, also known simply as *activation*, quantifies to which extent neuron j is currently *active* or *excited*. This is determined by the activation function

$$f_{\text{act}}(u_j; \theta_j) = f_{\text{act}}\left(\sum_{k=1}^{m} w_{s_k,j} y_{s_k}; \theta_j\right)$$

which combines the weighted input with the threshold $\theta_j \in \mathbb{R}$. There exist various choices for the activation function. In this work, the LeakyReLU activation function is chosen:

$$\text{LeakyReLU}(x) = \begin{cases} x, & \text{if } x \geq 0 \\ \text{negative\_slope} \times x, & \text{otherwise} \end{cases} \tag{4.5}$$

where negative_slope is the gradient of the negative part of the function that should be enough small [17]. Here negative_slope= 0.1.

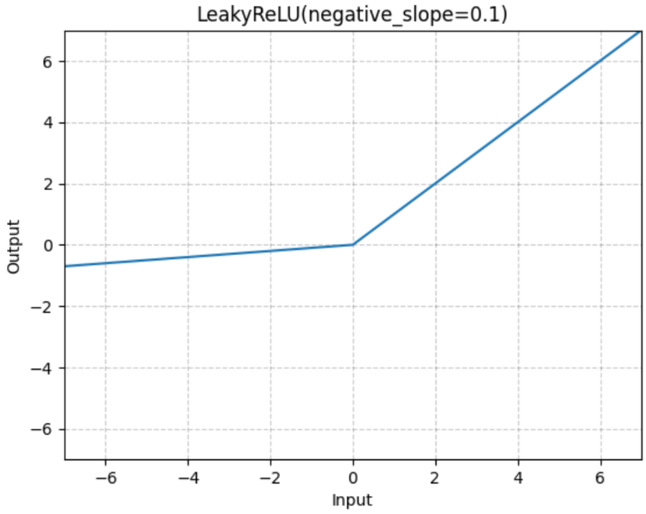

Figure 4.2: The activation function LeakyReLU with a negative slope of 0.1 [6].

To conclude, the output function f_{out} calculates the scalar output $y_i \in \mathbb{R}$ based on the activation state a_j of the neuron:

$$y_i = f_{\text{out}(a_j)}$$

Here, as it is often chosen, f_{out} is the identity function.

The connectivity of neurons inside a network determines the network's topology or architecture. Several network designs, often suited to a particular use, have been presented in the literature. In function regression tasks, *feedforward neural networks*, commonly known as *perceptrons* have been favoured over all others.
In a feedforward neural network, neurons are organized in layers, with one *input layer* of M_I source neurons, K *hidden layers* of H_k *computing neurons*, $k = 1, ...K$, and an *output layer* of M_O computing neurons. As a defining trait, neurons in a layer can only form connections with neurons in the subsequent output-facing layer. When an input vector $\mathbf{p} \in \mathbb{R}^{M_I}$ is provided to the network through the source nodes, the signal for the neurons in the first hidden layer is generated. The outputs of each hidden layer in turn feed the neurons in the subsequent layer. In this manner, information is sent to the output layer, whose outputs compose the components of the network's total output $\mathbf{q} \in \mathbb{R}^{M_O}$.
A feedforward network thereby creates a map between the input space R^{M_I} and the output space R^{M_O}. This makes this network design well-suited for approximating continuous functions. Indeed, multi-layer perceptrons (MLPs), i.e. NN with at least one hidden layer, as found in [21] and [22] by Cybenko, satisfy the following properties:

i) MLPs with one hidden layer and differentiable activation functions can approximate any continuous function;

ii) MLPs with two hidden layers and differentiable activation functions can approximate any function.

Hence, there is no need to deploy MLPs with more than two hidden layers in many practical situations. Unfortunately, (*i*) and (*ii*) do not provide any practical recommendations for either the number of hidden neurons or the number of samples necessary to train the network; these values must be determined by a trial-and-error approach.

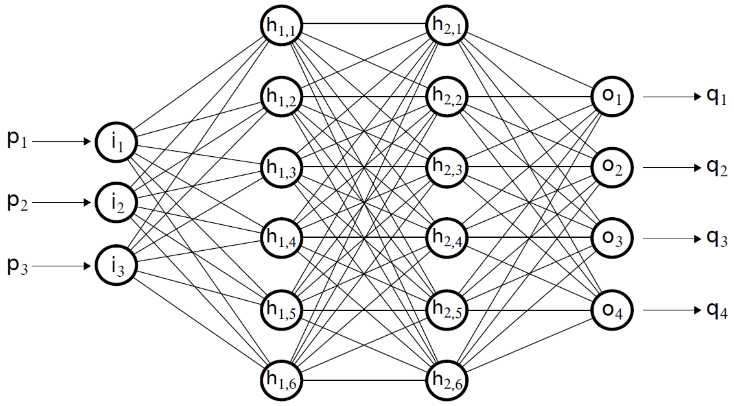

Figure 4.3: A three-layer feedforward neural network consisting of three input neurons, two hidden layers of six neurons each, and four output neurons. Within each link, the flow of information is left to right [35].

4.3.2. Direct Problem

In this section, we specify what is presented in the previous section. Namely, the neural network used in this phase is a map $\mathbf{NN}_\theta : \mathbb{R}^{N_\mathcal{P}+1} \to \mathbb{R}^{N_\theta^{\mathrm{POD}}}$ which retrieve from a set of parameter $\mathcal{P} = [\nu, M_0, \kappa, \delta, \delta_n, S_n]$ of cardinality $N_\mathcal{P}$ (given in Section 3.2), the coefficient of the basis function of the reduces space with dimension N_{POD} for the variable (see Algorithm 4.1). Here, we take a collection of inputs for each set in $\mathcal{P}$ completed with a specific time parameter. In such a way, we obtain the input vector $\mathcal{P}_t = [\nu, M_0, \kappa, \delta, \delta_n, S_n, t]$ where $[\nu, M_0, \kappa, \delta, \delta_n, S_n] \in \mathcal{P}_{\mathrm{bio}}$ and $t = 0, ..., T$, with T is the final time-step. The associated output is the list of coefficients of the solution projected on the ROM space at time t, i.e. $\{a_{\theta i}^t\} \in \mathbb{R}^{N^{\mathrm{POD}}}$. Having these coefficients $\{a_{\theta i}^t\}$, it is possible to retrieve the whole solution at time t through:

$$\phi_h^t = \sum_{i=1}^{N_{\mathrm{POD}}} a_{\phi i}^t \xi_i^\phi, \quad \mu_h^t = \sum_{i=1}^{N_{\mathrm{POD}}} a_{\mu i}^t \xi_i^\mu, \quad n_h^t = \sum_{i=1}^{N_{\mathrm{POD}}} a_{n i}^t \xi_i^n. \tag{4.6}$$

The training is performed on a data set of N_{Data} input-output pair that is split into a train set with N_{Train} elements, that is about $70-80\%$ of the whole data set, and a test set with N_{Test} elements, with the remaining instances of the data set. The values for each simulation are specified in the presentation of the numerical results (Chapter 5).

For all the cases we exhibit, the specific propagation, activation and output functions are selected to be the ones presented in 4.3.1, i.e. the weighted sum for the propagation function, the LeakyReLU as the activation function and just the identity for the output function. Moreover, the loss function used is the mean squared error $\mathbf{e}$ defined as:

$$\mathbf{e} = \frac{1}{n}\sum_{i=1}^{n}\left(Y_i - \hat{Y}_i\right)^2 \tag{4.7}$$

where Y_i is the vector of observed values of the variable being predicted, $\hat{Y}_i$ is its predicted value, and n is the number of data on which we are computing the error on. The minimization algorithm used, which objective is to detect the minimum of the loss function $\mathbf{e}$, is the *Limited-memory Broyden–Fletcher–Goldfarb–Shanno* algorithm (L-BFGS) [42].

Algorithm 4.1 Direct Problem Algorithm

```
Require: MRI$(t=0)$, DTI$(t=0)$, $\{\xi_s^\phi\}_{s=1,\dots,N_{\text{POD}}}$
for $k$ in range $(1, N_{\text{Simulations}})$ do
    $\mathcal{P}_k = [\nu_k, M_{0k}, \kappa_k, \delta_k, \delta_{nk}, S_{nk}] \leftarrow$ rand$(\mathcal{P}_{\text{bio}})$; #Pick a random parameters set
    Perform $\phi_k \leftarrow$ FOM(Initialization, $\mathcal{P}_k$); #Solve FOM given i.c. and parameters
    for $t$ in range $(1, N_{\text{Steps}})$ do
        $[a_1^t, \dots, a_{N_{\text{POD}}}^t] \leftarrow$ Projection$(\phi_k(t), \{\xi_s^\phi\})$; #Project phi on the ROM basis
        $(M_{\text{Output}})_{N_{\text{Steps}}(k-1)+t} = [\nu_k, M_{0k}, \kappa_k, \delta_k, \delta_{nk}, S_{nk}, t]$;
        $(M_{\text{Input}})_{N_{\text{Steps}}(k-1)+t} = [a_1^0, \dots, a_{N_{\text{POD}}}^0, a_1^T, \dots, a_{N_{\text{POD}}}^T]$;
    end for
end for
Training Phase NN$_\phi$ :
    $N_{\text{Train}} = 0.75 N_{\text{Data}}$;
    Train $\leftarrow M_{\text{Input}}[1 : N_{\text{Train}}]$, $M_{\text{Output}}[1 : N_{\text{Train}}]$;
    Test $\leftarrow M_{\text{Input}}[N_{\text{Train}}+1 : N_{\text{Data}}]$, $M_{\text{Output}}[N_{\text{Train}}+1 : N_{\text{Data}}]$;
Compute $[a_1^t, \dots, a_{N_{\text{POD}}}^t] \leftarrow$ NN$_\phi$ $(\nu, M_0, \kappa, \delta, \delta_n, S_n, t)$
```

4.3.3. Inverse Problem

The final objective of this methodology is the resolution of an inverse problem, that is the prediction of the patient-specific parameters of a clinical case starting from a pair of images obtained via the techniques presented in Chapter 2.

To achieve this aim, until this point, we have proposed a method able to speed up the computational time of the resolution of the direct problem. It is indeed fundamental to simulate several possible evolutions of the tumour growth, starting from a given initial condition, if we want to trace back the parameters that entail the specific evolution that comprises the actual distribution of tumour retrieved from the images.

Motivated by the results of the direct problem, which are obtained via a neural network that ensures a satisfyingly precise solution while drastically cutting drastically computational costs, it is reasonable to apply the same method for the inverse problem. Namely, we try once again to properly train a different neural network able to map the pair of tumour distributions projected onto the ROM space into the parameter space $\mathcal{P}_{\text{bio}}$.

Exploiting the features of the Reduced Order Model, which relies on very few degrees of freedom with respect to the FOM, we can, indeed, construct an input vector that embodies the information given by non-consecutive snapshots of the evolution of the tumour in the brain.

The approach we followed consists in starting from the results of two different brain tumour states, at times t_0 and t_1, which can be represented in the Full Order Space, i.e. $\phi(t_0)$ and $\phi(t_1)$ (see Algorithm 4.2). At this point, the two solutions can be projected on the Reduced Order Space obtaining the coefficients $\{\alpha^{t_0}_{\phi 1}, ..., \alpha^{t_0}_{\phi N_{\text{POD}}}\}$ from $\phi(t_0)$ and $\alpha^{t_1}_{\phi 1}, ..., \alpha^{t_1}_{\phi N_{\text{POD}}}$ from $\phi(t_1)$.

Then the coefficients are concatenated in a single vector containing the information of both of the snapshots $[\alpha^{t_0}_{\phi 1}, ..., \alpha^{t_0}_{\phi N_{\text{POD}}}, \alpha^{t_1}_{\phi 1}, ..., \alpha^{t_1}_{\phi N_{\text{POD}}}] \in \mathbb{R}^{2N^{\text{POD}}_{\phi}}$ that is the input of this neural network.

With this information, a map $\mathbf{NN}_{\text{inv}}$ between the concatenated vector of the coefficients of the two time-steps and the specific parameters $[\nu, M_0, \kappa, \delta, \delta_n, S_n] \in \mathcal{P}_{\text{bio}}$ relating to the same patient can be defined. Namely, we train a neural network $\mathbf{NN}_{\text{inv}} : \mathbb{R}^{2N^{\text{POD}}_{\phi}} \to \mathbb{R}^{N_{\mathcal{P}}}$ which approximate this map. Specifically:

$$(\nu, M_0, \kappa, \delta, \delta_n, S_n) = \mathbf{NN}_{\text{inv}} \left(\alpha^{t_0}_{\phi 1}, ..., \alpha^{t_0}_{\phi N_{\text{POD}}}, \alpha^{t_1}_{\phi 0}, ..., \alpha^{t_1}_{\phi N_{\text{POD}}} \right).$$

Where t_0 is the time-step of the first snapshot while t_1 is the one of the second snapshots.

Once again, the training is performed on a data set of N_{Data} input-output pair that is split into a train set with N_{Train} elements, that is about $70 - 80\%$ of the whole data set, and a test set with N_{Test} elements, with the remaining instances of the data set. The values for each simulation are specified in the presentation of the numerical results (Chapter 5).

For all the cases we exhibit, the specific propagation, activation and output functions are selected to be the ones presented in 4.3.1, i.e. the weighted sum for the propagation function, the LeakyReLU as the activation function and just the identity for the output function. Moreover, the loss function used is the mean squared error $\mathbf{e}$ defined in 4.7. The minimization algorithm used is L-BFGS.

Algorithm 4.2 Inverse Problem Algorithm

```
Require: $\mathrm{MRI}(t=0), \mathrm{DTI}(t=0), \mathrm{MRI}(t=T), \mathcal{P}_{\text{target}}, \{\xi_s^\phi\}_{s=1,\dots,N_{\text{POD}}}$
for $k$ in range $(1, N_{\text{Data}})$ do
    $\mathcal{P}_k \leftarrow$ rand($\mathcal{P}_{\text{bio}}$); #Pick a random set of parameters
    Perform $\phi_k \leftarrow$ FOM(Initialization, $\mathcal{P}_{\mathbf{k}}$);#Solve FOM given i.c. and parameters
    $\left[a_1^0, \dots, a_{N_{\text{POD}}}^0\right] \leftarrow$ Projection($\phi_k(t=0), \{\xi_s^\phi\}$);#Project phi on the ROM basis
    $\left[a_1^T, \dots, a_{N_{\text{POD}}}^T\right] \leftarrow$ Projection($\phi_k(t=T), \{\xi_s^\phi\}$);
    $(M_{\text{Output}})_k = [\mathcal{P}_k]$;
    $(M_{\text{Input}})_k = \left[a_1^0, \dots, a_{N_{\text{POD}}}^0, a_1^T, \dots, a_{N_{\text{POD}}}^T\right]$;
end for
Training Phase $\mathbf{NN}_{\text{inv}}$ :
    $N_{\text{Train}} = 0.75 N_{\text{Data}}$;
    Train $\leftarrow M_{\text{Input}}[1 : N_{\text{Train}}]$, $M_{\text{Output}}[1 : N_{\text{Train}}]$;
    Test $\leftarrow M_{\text{Input}}[N_{\text{Train}} + 1 : N_{\text{Data}}]$, $M_{\text{Output}}[N_{\text{Train}} + 1 : N_{\text{Data}}]$;
Compute $\mathcal{P}_{\text{guess}} \leftarrow \mathbf{NN}_{\text{inv}}\left(a_1^0, \dots, a_{N_{\text{POD}}}^0, a_1^T, \dots, a_{N_{\text{POD}}}^T\right)$
```

5 | Numerical Results

In this Chapter, we run through all the steps of the numerical simulations that lead to the final results. The overall implementation framework exploits the functionalities given by the platform `FEniCSx` which is a popular open-source framework for solving partial differential equations. The implementation of the used code heavily relies on two of its components:

- `Dolfinx`, a C++/Python library providing data structures and algorithms for finite element meshes, automated finite element assembly, and numerical linear algebra [1];
- Unified Form Language `UFL` which is a domain-specific language for declaration of finite element discretizations of variational forms. More precisely, it defines a flexible interface for choosing finite element spaces and defining expressions for weak forms in a notation close to mathematical notation [2].

All codes are parallelized and the time specifics showed in the following sections rely on a multi-thread CPU with 20 cores.

5.1. Patient Specific Parameters Estimation on a Two-Dimensional Geometry

In this section, we test the whole process to retrieve the parameter of the model specific to a singular patient on a two-dimensional mesh.

As we have stated in Chapter 4, in order to compute patient-specific parameters, a reduction of the degrees of freedom of the problem is needed if we ask for a result in a reasonable time. The pathway that we have followed in this work is to face the direct problem of computing the solution given the parameters in a restricted amount of time by exploiting a reduced basis method that exploits the POD for the construction of the reduced space. In such a way we can compute a great number of reduced solutions, starting from randomly picked parameters, that are useful to enlarge our data set of fictitious clinical cases. The construction of the ROM basis is obtained through `RBniCSx` [36], a library useful to implement reduced-order modelling techniques.

Then, we can train a neural network to map the inverse problem. Starting from the reduced solution obtained in the previous step indeed, we can simulate the real evolution of a GBM by following the procedure exposed in Section 4.3.3. The starting point in the real case is the collection of two functions obtained by a chosen image technique that are then projected onto the reduced space and subsequently concatenated to form the input vector.

5.1.1. Direct Problem

To compute a solution in a feasible time it is important to reduce the degrees of freedom of the spaces we want to find the solution in. As described in Chapter 4, Proper Orthogonal Decomposition is a suitable technique to pursue this aim.

Unfortunately, as it is shown below, the classical approach which entails the projection of the operators on the ROM basis, without an interpolation method which approximates the nonlinear convex term in the double-well potential (such as DEIM), does not improve the time effort.

For this reason, here we take advantage of one of its variations, POD-NN, which exploits a neural network $\mathbf{NN}_\phi$ to approximate the map between the parameter and the coefficient of the function representing the concentration of tumour obtained after its projection of the ROM space. POD-NN make it possible to overcome the projection of the operators cutting drastically computational costs.

In this case, the basis is built up starting from $M = 32$ set of different parameters and we have put the dimension of the ROM basis to $N_{\text{POD}} = 30$. This is due to μ that, as it is shown in Table 5.1, requires a ROM space of greater dimension in order to make POD technique precise, with respect to ϕ and n that could only rely on about ten element for the base to keep the same $ic \approx 0.95$. This dependency on the number of basis N_{POD} introduce a trade-off between the accuracy of the Reduced Order Model and its computational effort.

With the POD-NN approach, a greater basis entails a negligible computational effort in terms of the computation of the reduced order solution since the projection operation is still of the order of seconds. On the other hand, it increases the degree of freedom of the ROM nullifying our objective of reduction that is fundamental to ensure that the training can be done on simple neural networks in few time.

Furthermore, we observe that improve accuracy becomes useless from a point on, since the shape and dimension of the tumour are well traced even if some oscillation arouses (see Figure 5.3).

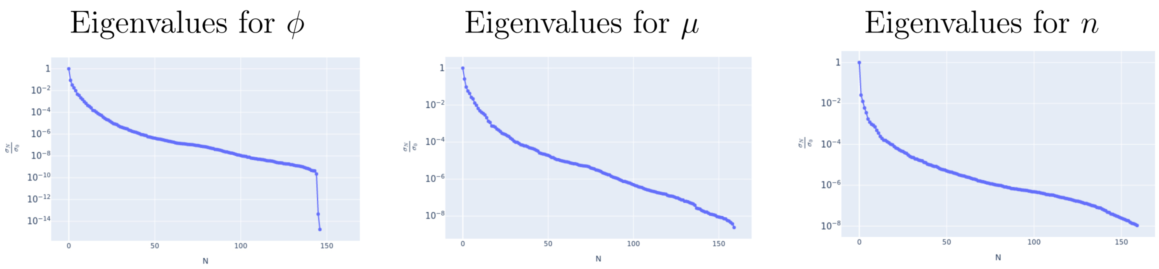

Table 5.1: Ratio of ordered eigenvalues over the greatest of them for the physical variables ϕ, μ and n over the square mesh.

Once we have fixed the dimension of the Reduced Order Space, it is possible to reproduce multiple simulations to build up a data set big enough for training the neural network $\mathbf{NN}_\phi$. Here, the number of data points is $N_{\text{Data}} = 45000$ divided in $N_{\text{Train}} = 33000$ training points and $N_{\text{Test}} = 12000$ testing points. The neural network $\mathbf{NN}_\phi$ consists of 3 layers of 50 nodes each. In Fig. 5.1 the train and test absolute errors, computed as the mean error $\mathbf{e}$ respectively on the test and on the trial, are exhibited.

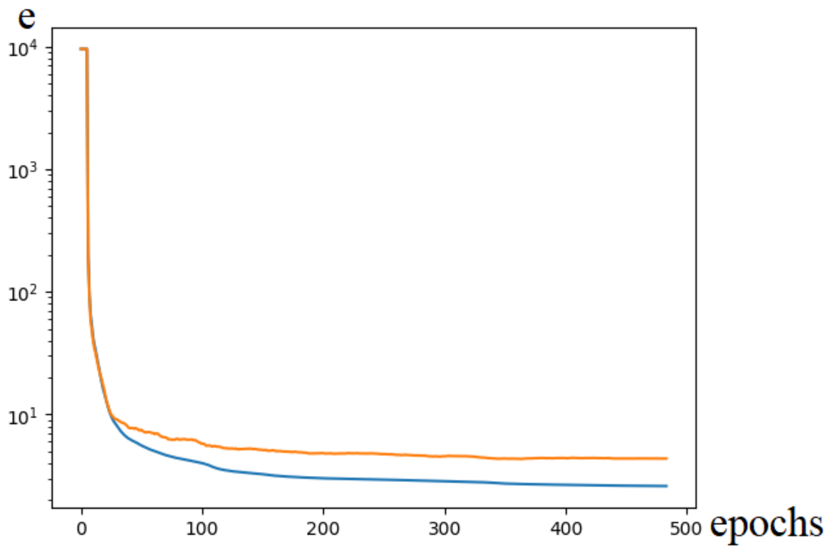

Figure 5.1: Absolute mean square error $\mathbf{e}$ over the epochs in the training of the neural network $\mathbf{NN}_\phi$. The error over the train set is coloured in blue while the error over the test set is coloured in orange.

5.1.2. Inverse Problem

Starting from a large number of reduced solutions it is possible to train the map $\mathbf{NN}_{\text{inv}}$. Here again, we exploit a 3-layer neural network, where each layer is of 50 neurons, for the propagation function the weighted sum, as activation function the LeakyReLU and just the identity for the output function.

Has specified in Section 4.3.3, here we construct the input data as the collection of the coefficient of two snapshots, obtaining a vector $[\alpha^{t_0}_{\phi 1}, ..., \alpha^{t_0}_{\phi N_{\text{POD}}}, \alpha^{t_1}_{\phi 1}, ..., \alpha^{t_1}_{\phi N_{\text{POD}}}] \in \mathbb{R}^{2N^{\text{POD}}_{\phi}}$ for each set of parameters $\mathcal{P}$.

The number of data points, in this case, is $N_{\text{Data}} = 22500$ divided in $N_{\text{Train}} = 16500$ training points and $N_{\text{Test}} = 6000$ testing points. The results in terms of error are exhibited in Fig.5.2.

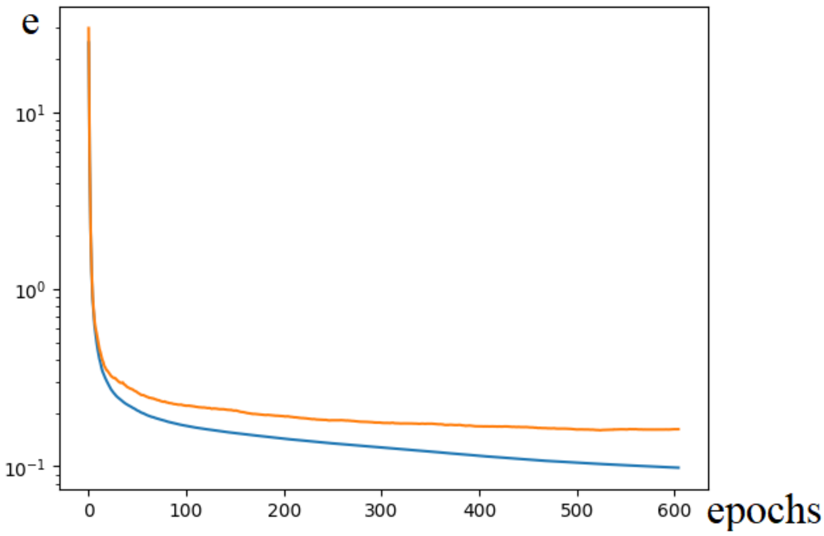

Figure 5.2: Relative mean square error $\mathbf{e}$ over the epochs in the training of the neural network $\mathbf{NN}_{\text{inv}}$. The error over the train set is coloured in blue while the error over the test set is coloured in orange.

5.1.3. Estimation results

This section is a comparison of the evolution of the concentration of tumour over time in terms of shape and computational time effort over a square of dimension 100 × 100 mm with a mesh of triangular-shaped elements. Starting from this set of parameter

$$(\nu, M_0, \kappa, \delta, \delta_n, S_n) = (0.26132, 3823.48, 732.125, 0.30654, 26951.7, 69628.5) \tag{5.1}$$

we retrace all the steps described before.

We have placed the tumour at the centre of the domain as a circle of radius $\sqrt{10}$ mm. So the initial condition reads:

$$\phi_0(x, y) = \mathbb{I}_\Omega \quad \text{where } \Omega = \{x, y \in \mathbb{R}^2 \text{ s.t. } (x - 50.0)^2 + (y - 50.0)^2 < 10.0\}$$

Tensor T is of the form $\mathsf{T} = [[3.0, 0.0], [0.0, 1.0]]$ to let the tumour grow faster along the horizontal direction. The temporal interval T comprises 100 days.

From this, simulating the FOM solution over time with different sets of parameters picked from the biological range $\mathcal{P}_{\text{bio}}$. With enough snapshots (here we have simulated M=32 different sets of parameters), it is possible to construct the ROM basis via the POD method. As we said, the number of basis is $N_{\text{POD}} = 30$.

The next step is to simulate with random parameters (in this case 900 simulations) the Reduced Order problem retrieving an adequate amount of coefficient for the reduced basis. In such a way, we have constructed a data set big enough to train the map $\mathbf{NN}_\phi$ from the parameter of the model, plus the time-step, and the coefficient of the projected solution at that time-step. This method let us to compute the solution in a lower amount of time with respect to the FOM and ROM solutions (see Table 5.2).

After, we construct the data set for the inverse problem which holds fewer datapoints w.r.t the direct problem due to its complexity. Indeed, the inverse problem can only rely on a couple of time-steps of the whole simulation, while the direct problem takes information from all the steps, instead.

Actually, in order to enlarge our data set, we couple randomly pairs of snapshots equally distant in time. Namely, in this example, the simulation covers 100 days, so if we suppose we can take two clinical images 70 days apart, we can pretend the initial condition to be the distribution in one of the first 30 days and then take 70 days from that instant to see how the tumour has evolved. Choosing a timestep of $dT = 2$ days, we can rely on 15 couples of snapshots for each parameter set. $\mathbf{NN}_{\text{inv}}$ can be trained at this point as described in the previous section.

Given that, we imagine starting from two tumour distributions distant in time, and we obtain the patient-specific parameters in a time comparable to the resolution of the inverse neural network. For the set of parameters (5.1) we obtain these estimated parameters:

$$(\nu, M_0, \kappa, \delta, \delta_n, S_n) = (0.26168, 3643.48, 750.072, 0.30218, 25157.7, 86628.5) \tag{5.2}$$

which entail an evolution as in Figure 5.3 and 5.3.

Simulation	Elapsed time
Full Order Model	61.5 s
Reduced Order Model	310 s
Reduced Order Model - Neural Network	5 s

Table 5.2: Computational time for the different used techniques.

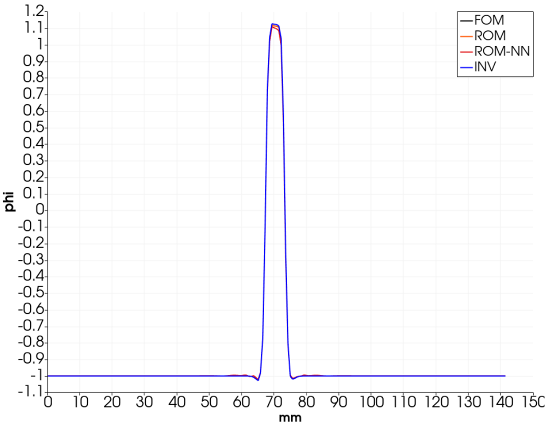

(a) **t=0**

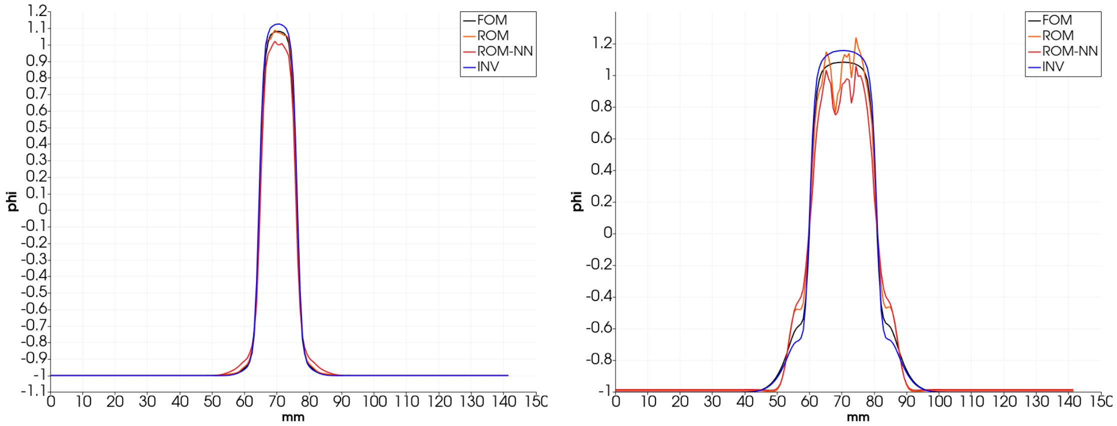

(b) **t=25**

(c) **t=50**

Figure 5.3: Evolution of a GMB. Plot of the solution ϕ along a straight line intersecting the tumour. From left to right, the plot for each used method at t$= 0, 25, 50$ time-steps is shown. In black, the solution computed via the Full Order Model; in orange, the solution computed via the classical Proper Orthogonal Decomposition; in red, the solution computed via the Neural Network variation of the POD; in blue, the solution computed via FOM starting from the parameter obtained in the inverse problem. FOM solution is indistinguishable from the one obtained via the inverse problem, entailing a good estimation of the parameter.

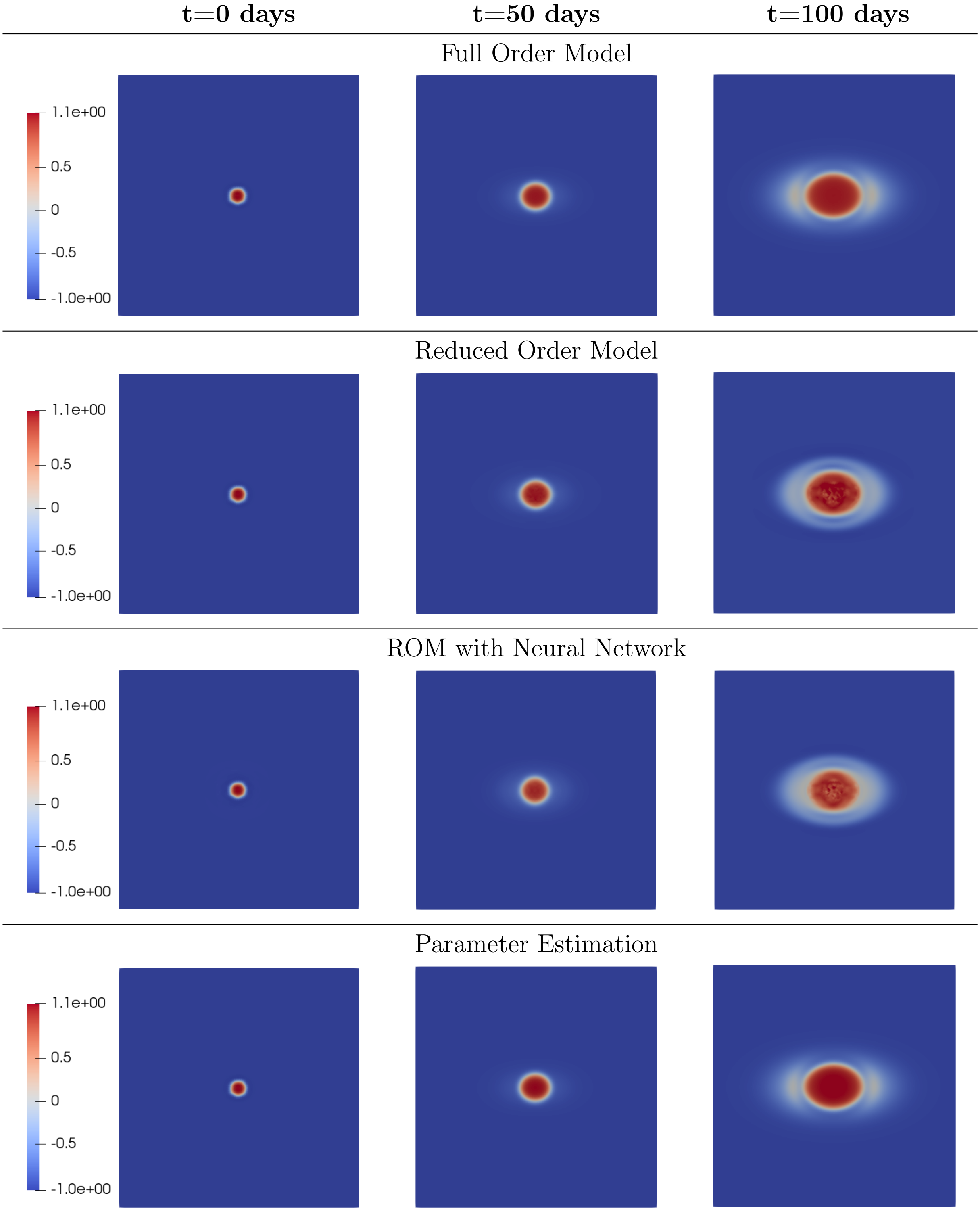

Table 5.3: Evolution of a GMB. From left to right, the solution ϕ for each used method at t$=0, 50, 100$ days are shown. From top to bottom: the solution computed via the Full Order Model; the solution computed via the classical Proper Orthogonal Decomposition; the solution computed via the Neural Network variation of the POD; the solution computed via FOM starting from the parameter obtained in the inverse problem.

5.2. Description of the used geometrical mesh and a FOM evolution

We start this section by presenting the mesh used in the simulations on the brain. In this work, we compute solutions over a realistic brain-shaped mesh with 32293 vertices and 196778 tetrahedral elements. The brain mesh is represented in Fig. 5.4. This domain represents a real clinical case obtained via MRI and DTI techniques, see Chapter 2. For each simulation, a piecewise linear basis function is chosen, so that the degrees of freedom of the solution corresponds to the number of vertices.

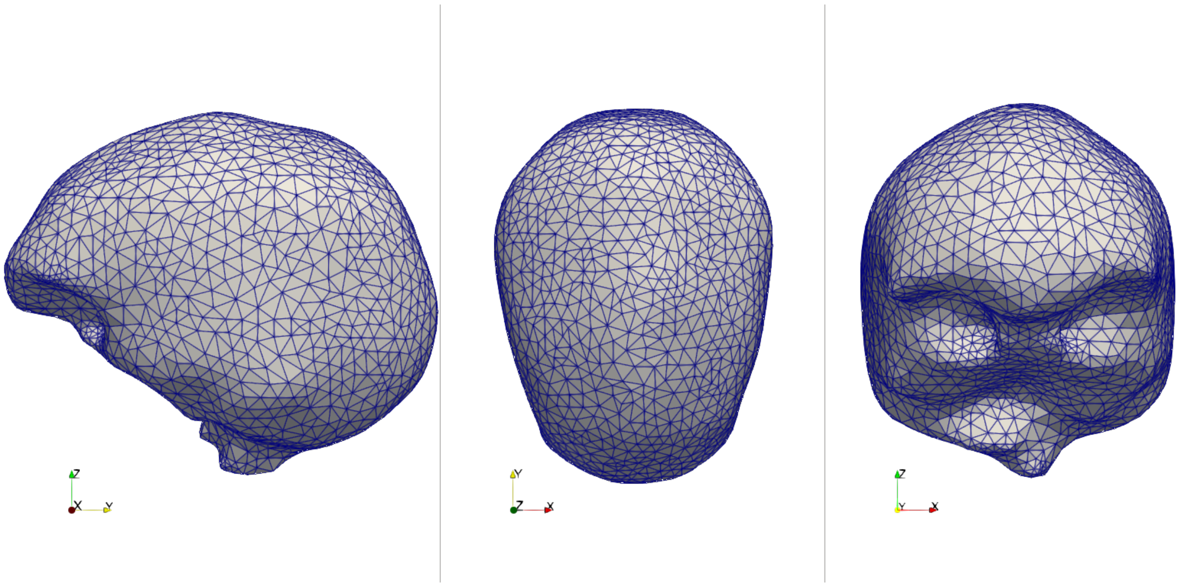

Figure 5.4: Brain mesh. Respectively sagittal, axial and coronal view

In order to capture with an adequate accuracy, the geometrical mesh is refined in the neighborhood where the tumour is placed in the initial instant. In such a way, we can have a better description in terms of tumour shape over time neglecting the dynamic far from it since the concentration vanishes at each time-step. In Figure 5.5 we exhibit the proposed mesh refinement that is compared with the actual placement of the tumour at initial state.

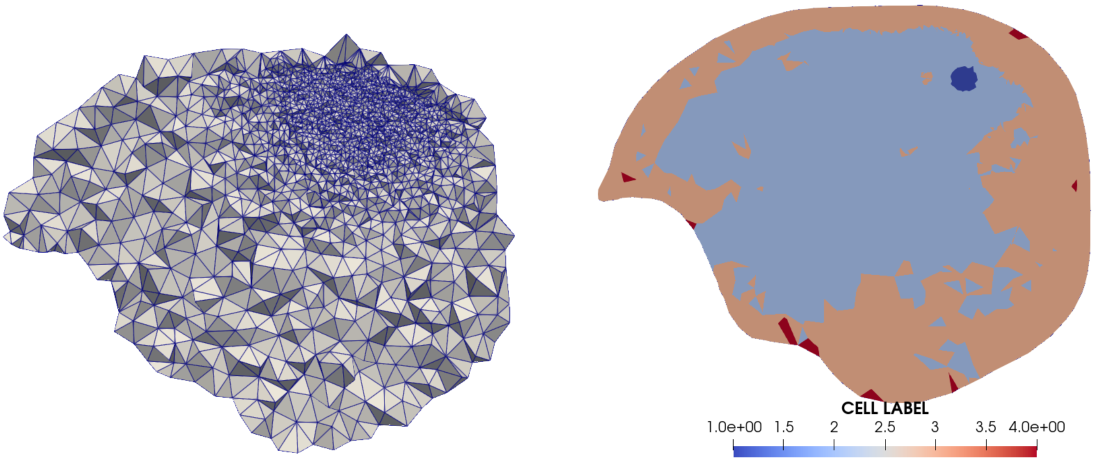

Figure 5.5: Sagittal section of the brain refined geometrical mesh. On the left, a view on the refinement applied in the neighbourhood of the tumour placement. On the right, the mesh labeled according to the different occupation zones. The area in blue (1.0) is that occupied by the tumour, in light blue (2.0) by the white matter, in ochre (3.0) by the grey matter and in red (4.0) by the cerebrospinal fluid.

Moreover, Diffusion Tensor Imaging gives us the information on how water diffuses into the various areas of the brain. Specifically, DTI provides information on both the intensity and directions of the movement of water molecules in the brain and such information is contained in the nutrient diffusion tensor D (Figure 5.6). Brain can obviously be represented as an anisotropic space such that a tensor is required to describe the diffusion since the probabilities of the molecule moving along the 3 orthogonal axes are neither identical nor independent. The same holds true for the tensor of tumour preferential motility T (Figure 5.7). Tensors are both symmetric, this means that we can rely on just six component to describe their three-dimensional distribution.

Given the mesh, we start computing the evolution of the Full Order Model described in section 3.6. In Table 5.4, the results at time-steps $t = 0, 30, 60$ are exhibited. In this case, the tumour is supposed to start from a globular shape centred in $(x, y, z) = (19.3, 30.8, 3.0)[\text{cm}]$ whose concentration ϕ_0 at initial time is distributed as :

$$\phi_0(x, y, z) = 2e^{-100((x-19.3)^2+(y-30.8)^2+(z-3.0)^2)^2} - 1$$

The parameters of the models are randomly picked in the parameters biological range $\mathcal{P}_{\text{bio}}$ presented in Section 3.5 are the following:

- $\nu = 0.373555\,\text{day}^{-1}$

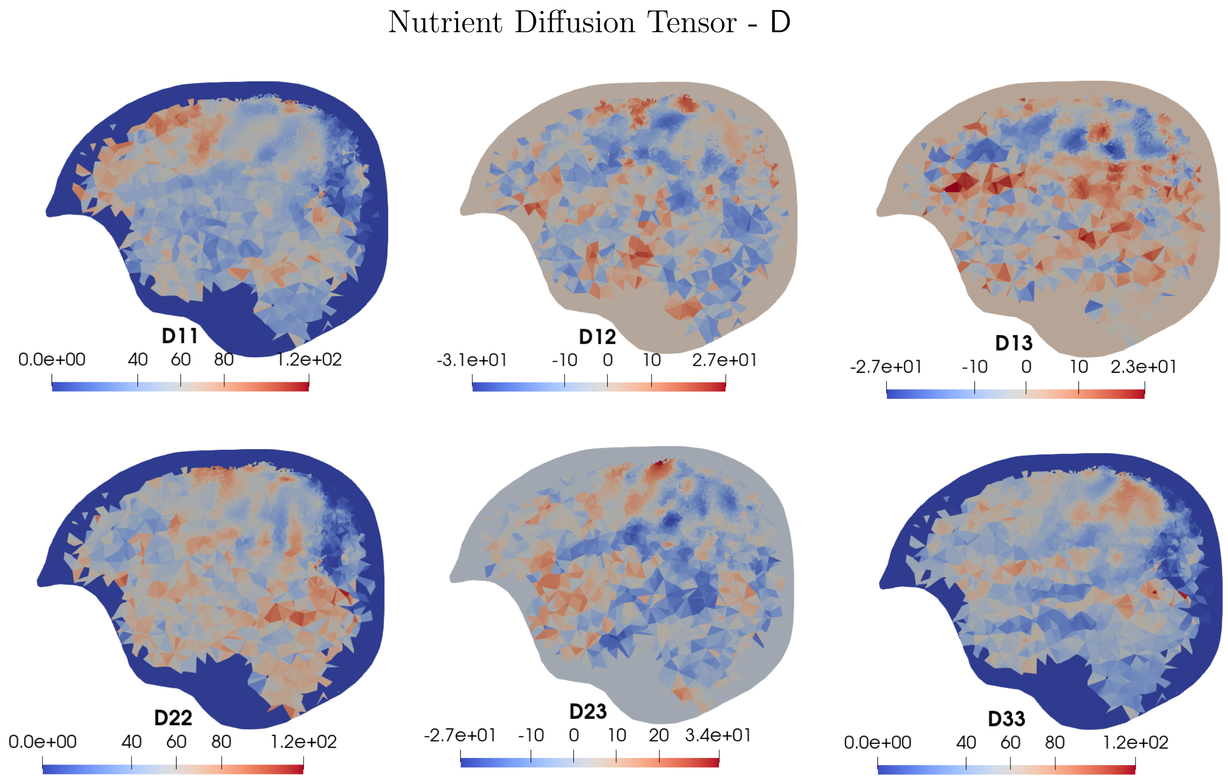

Figure 5.6: The six components of tumour preferential motility tensor D.

- $M_0 = 3330.444\,(\mathrm{Pa} \cdot \mathrm{day})/\mathrm{mm}^2$
- $k = 754.808\,\mathrm{Pa}$
- $\delta = 0.248254$
- $\delta_n = 12064.87\,\mathrm{day}^{-1}$
- $S_n = 40078.0\,\mathrm{day}^{-1}$

As we have seen in Chapter 1, GBM is a fast-growing tumour. It is, indeed, evident that in 60 time-steps, i.e. 30 days, its volume covers a dramatic portion of the whole brain. Moreover, the concentration of nutrient n complementary follows the behaviour of the tumour development as expected, being poor in the region where the concentration of tumour is higher while approximately 1 elsewhere, see Table 5.5.

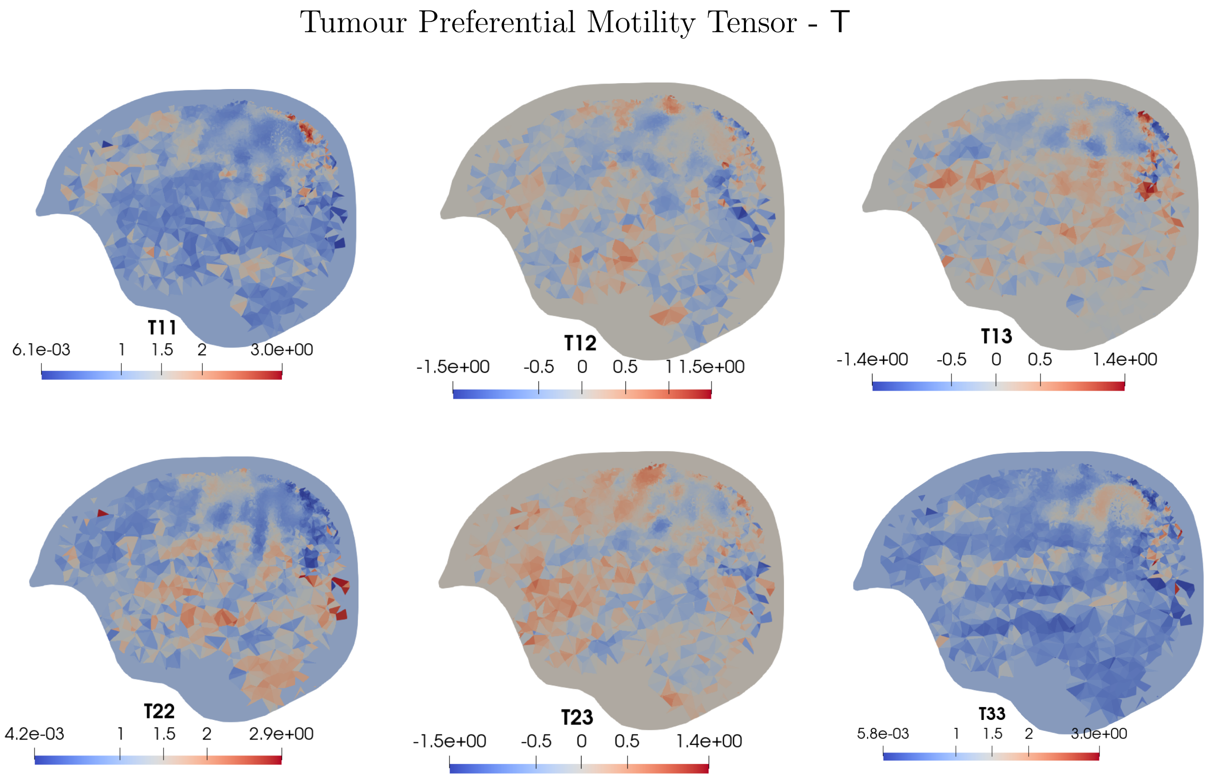

Figure 5.7: The six components of tumour preferential motility tensor T.

5.3. Patient Specific Parameters Estimation on a Real Domain

In this section, we follow the approach we used in the two-dimensional test case to retrieve the parameter of the model specific to a singular patient but on the real brain mesh we presented in Section 5.2

5.3.1. Direct Problem

We rely on the Proper Orthogonal Decomposition variation with Neural Network to approximate the map between the parameter and the coefficient of the function representing the concentration of tumour obtained after its projection of the ROM space. We remember that since POD-NN make it possible to overcome the projection of the operators, computational costs are drastically cut.

In this case, we construct a basis starting with a bigger set of parameters, in particular, we take $M = 64$ different sets. We have chosen even to enlarge the ROM basis to $N_{\text{POD}} = 40$ (first 6 elements are exhibited in Figure 5.8). Indeed, as it is shown in Table 5.6, μ

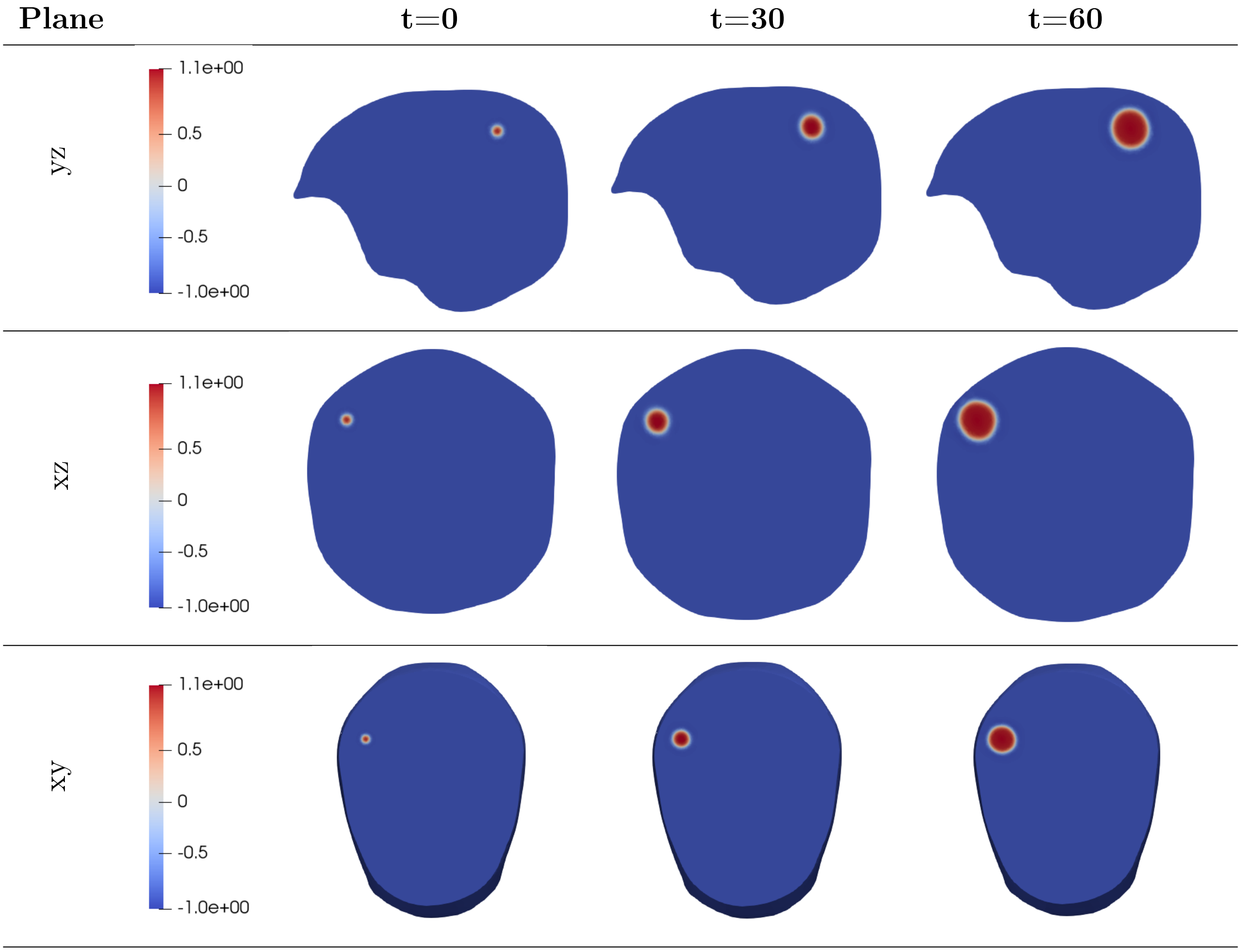

Table 5.4: Evolution of a GMB. From left to right, the solution for the Full Order Model of the concentration of tumour variable ϕ at t$=0, 15, 30$ days is shown. From top to bottom, sagittal, coronal and axial views at each time-step are exhibited.

requires a ROM space of greater dimension in order to make the POD technique precise, with respect to ϕ and n that could only rely on about ten elements for the base to keep the same $ic \approx 0.95$. As it can be seen in Figure 5.11, this choice ensures a better reduced solution in the sense that it follows almost completely the original FOM solution without to many oscillations.

Once we have fixed the dimension of the Reduced Order Space, it is possible to reproduce multiple simulations to build up a data set big enough for training the neural network $\mathbf{NN}_\phi$. Here, the number of data points is $N_{\text{Data}} = 45000$ divided in $N_{\text{Train}} = 33000$ training points and $N_{\text{Test}} = 12000$ testing points. The neural network $\mathbf{NN}_\phi$ consist of 3 layer of 100 nodes each. In Fig. 5.9 the train and test absolute errors, computed as the mean square distance, are exhibited.

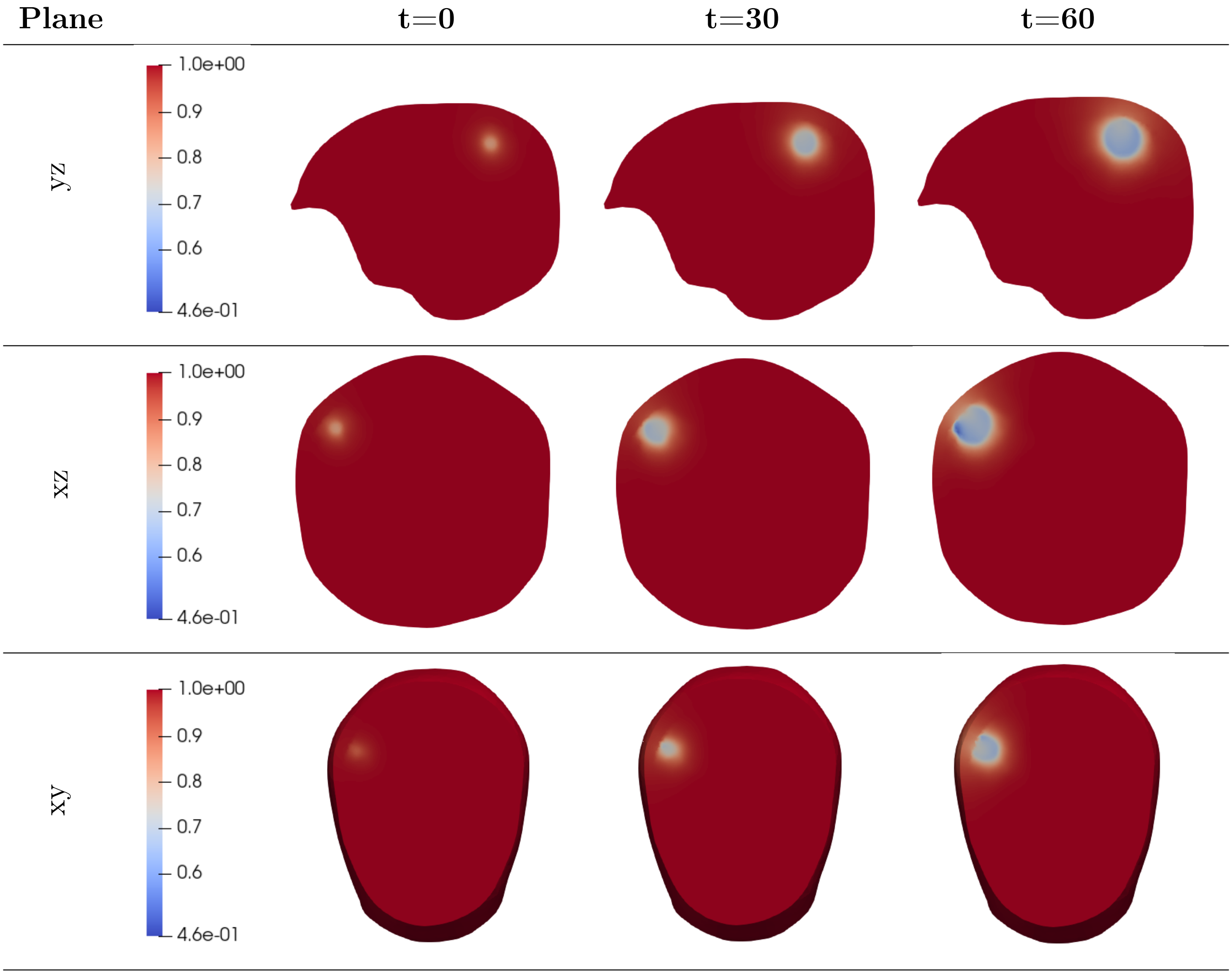

Table 5.5: Evolution of a GMB. From left to right, the solution for the Full Order Model of the concentration of nutrient variable n at t$=0, 15, 30$ days is shown. From top to bottom, sagittal, coronal and axial views at each time-step are exhibited.

5.3.2. Inverse Problem

Starting from a large number of reduced solutions it is possible to train the map $\mathbf{NN}_{\text{inv}}$. Here, we have built up a 3-layer neural network, where each layer is of 100 neurons. The specific propagation, activation and output functions are selected to be the ones presented in 4.3.1, i.e. the weighted sum for the propagation function, the LeakyReLU as the activation function and just the identity for the output function. We infer as in the test case to build up a proper data set. Namely, in this example, the simulation covers 30 days, so if we suppose we can take two clinical images 20 days apart, we can pretend the initial condition to be the distribution in one of the first 10 days and then take 20 days from that instant to see how the tumour has evolved. Since we have chosen a timestep of

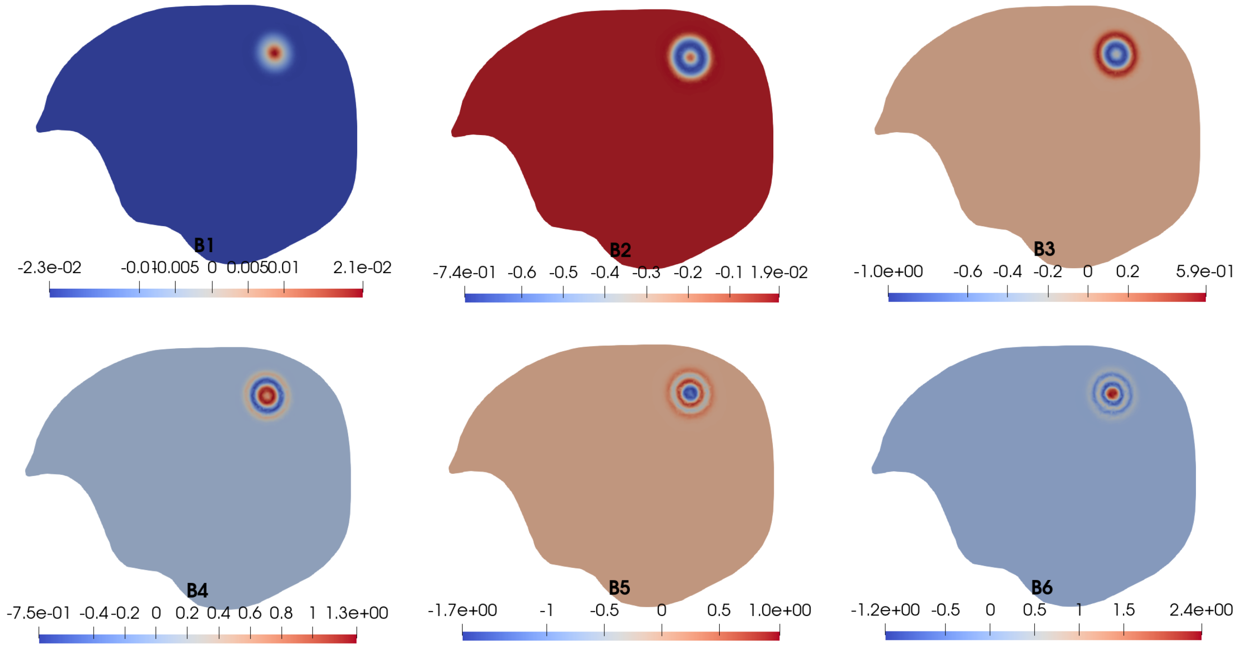

Figure 5.8: The first six elements (out of $N_{\text{POD}} = 40$) of the reduced order model basis for the tumour concentration variable ϕ.

$dT = 0.5$ days, we can rely on 20 couples of snapshots for each parameter set. $\mathbf{NN}_{\text{inv}}$ can be trained at this point as described in the previous section.

In 5.10, we can see how the train and the trial relative errors decrease. It can be observed that both trail and test relative mean square error flatten around 0.15.

Although this result appears to be non-optimal in order to catch the exact parameter of a patient, the following simulations show that the specific behaviour is actually well captured. This is mainly due to the little sensitivity of some of the parameters, for which, even if the predicted values have a non-negligible deviation from the actual ones, the consequent tumour spreading is not so affected in terms of precision of tracking the actual solution.

5.3.3. Estimation results

This section is a comparison of the evolution of the concentration of tumour over time in terms of shape and computational time effort. Starting from this set of parameter

$$(\nu, M_0, \kappa, \delta, \delta_n, S_n) = (0.35605, 3860.68, 700.390, 0.24015, 21041.0, 41978.3) \tag{5.3}$$

we retrace all the steps described in previous Chapters.

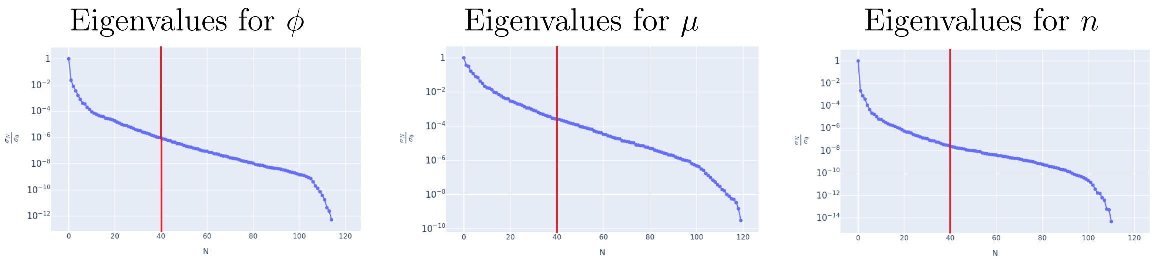

Table 5.6: Ratio of ordered eigenvalues over the greatest of them for the physical variables ϕ, μ and n over the brain mesh.

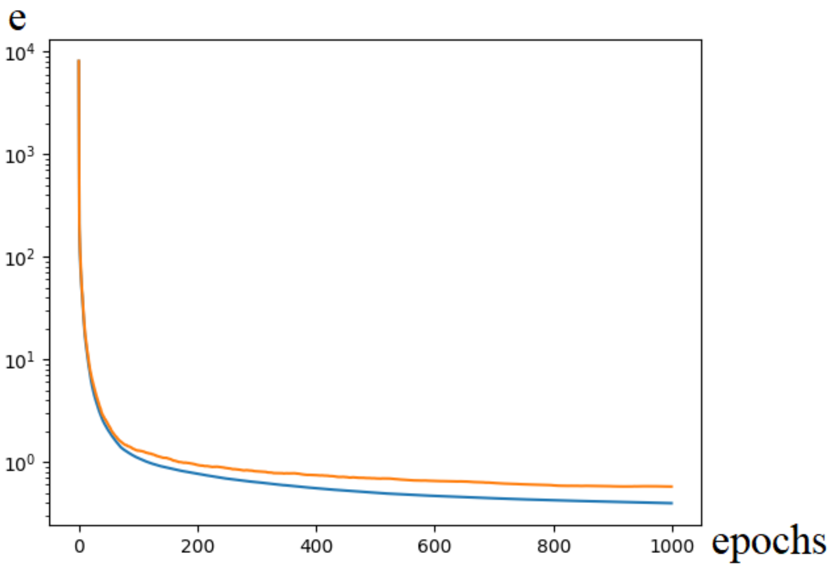

Figure 5.9: Absolute mean square error **e** over the epochs in the training of the neural network $\mathbf{NN}_\phi$. The error over the train set is coloured in blue while the error over the test set is coloured in orange.

Emulating a clinical case, after a first Magnetic Resonance Imaging, we suppose the patient to start from a globular tumour mass distributed as

$$\phi_0(x, y, z) = 2e^{-100((x-193)^2+(y-308)^2+(z-30)^2)^2} - 1.$$

where spatial quantities are expressed in mm. From this, simulating the FOM solution over time with different sets of parameters picked from the biological range $\mathcal{P}_{\text{bio}}$. With enough snapshots (here we have simulated $M = 64$ different sets of parameters), it is possible to construct the ROM basis via the POD method. As we said, the number of basis is $N_{\text{POD}} = 40$.

The next step is to simulate with random parameters (in this case 750 simulations) the

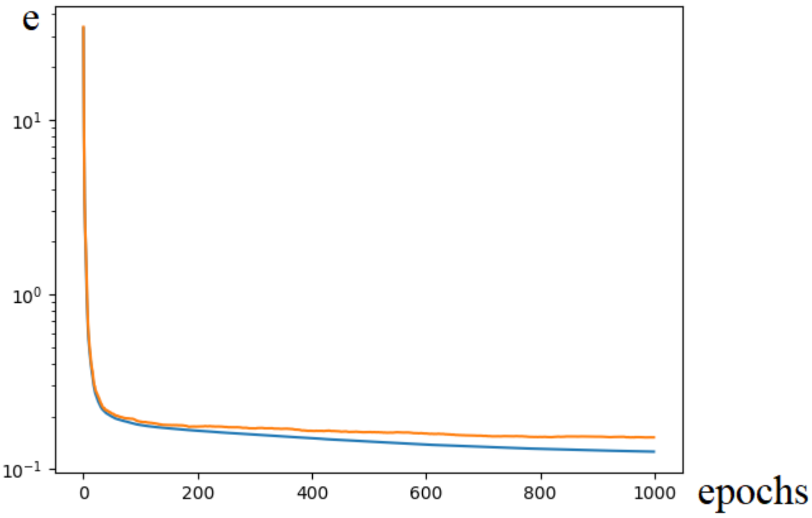

Figure 5.10: Relative mean square $\mathbf{e}$ over the epochs in the training of the neural network $\mathbf{NN}_{\text{inv}}$. The error over the train set is coloured in blue while the error over the test set is coloured in orange.

Reduced Order problem retrieving an adequate amount of coefficient for the reduced basis. Since the ROM solution using POD without the neural network variation takes much more time to be computed, as can be seen in Table 5.7, we prefer to simulate the FOM and then project over the reduced basis. In such a way, we have constructed a data set big enough to train the map $\mathbf{NN}_\phi$ from the parameter of the model, plus the time-step, and the coefficient of the projected solution at that time-step.

Once again, we train $\mathbf{NN}_{\text{inv}}$ as explained in the previous subsection.

Given that, we are ready for the patient to take a second MRI, from which we can obtain the patient-specific parameters in a time comparable to the resolution of the inverse neural network. For the set of parameters (5.3) we obtain these estimated parameters:

$$(\nu, M_0, \kappa, \delta, \delta_n, S_n) = (0.36982, 3950.38, 776.890, 0.25159, 25142.4, 36982.5) \tag{5.4}$$

which entail an evolution as in Figure 5.11 and Table 5.8. As we can see in Figure 5.11d, the volume fraction is well-tracked over time entailing a good estimation both in terms of tumour morphology.

Simulation	Elapsed time
Full Order Model	920 s
Reduced Order Model	5190 s
Reduced Order Model - Neural Network	5 s

Table 5.7: Computational time for the different used techniques.

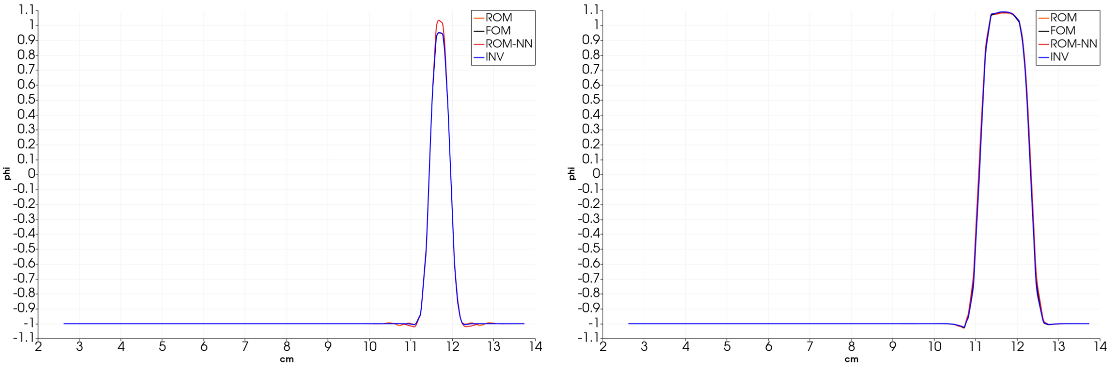

(a) **t=0 days** (b) **t=15 days**

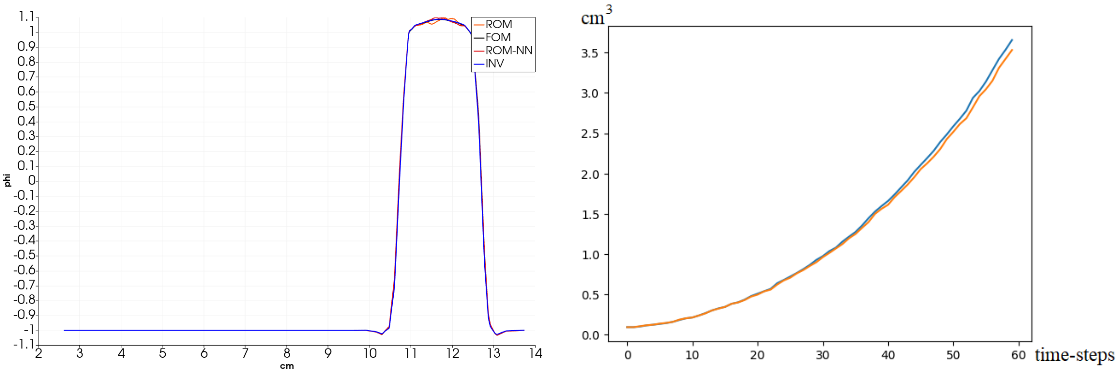

(c) **t=30 days** (d) Volume fraction over time

Figure 5.11: Evolution of a GMB. Plot of the solution ϕ along a straight line intersecting the tumour (a),(b)and (c). The plot for each used method at t$=0, 15, 30$ days is shown. In black, the solution computed via the Full Order Model; in orange, the solution computed via the classical Proper Orthogonal Decomposition; in red, the solution computed via the Neural Network variation of the POD; in blue, the solution computed via FOM starting from the parameter obtained in the inverse problem. FOM solution is indistinguishable from the one obtained via the inverse problem, entailing a good estimation of the parameter.
In (d), the volume fraction of tumour over time. In blue, the actual evolution; in orange, the predicted one.

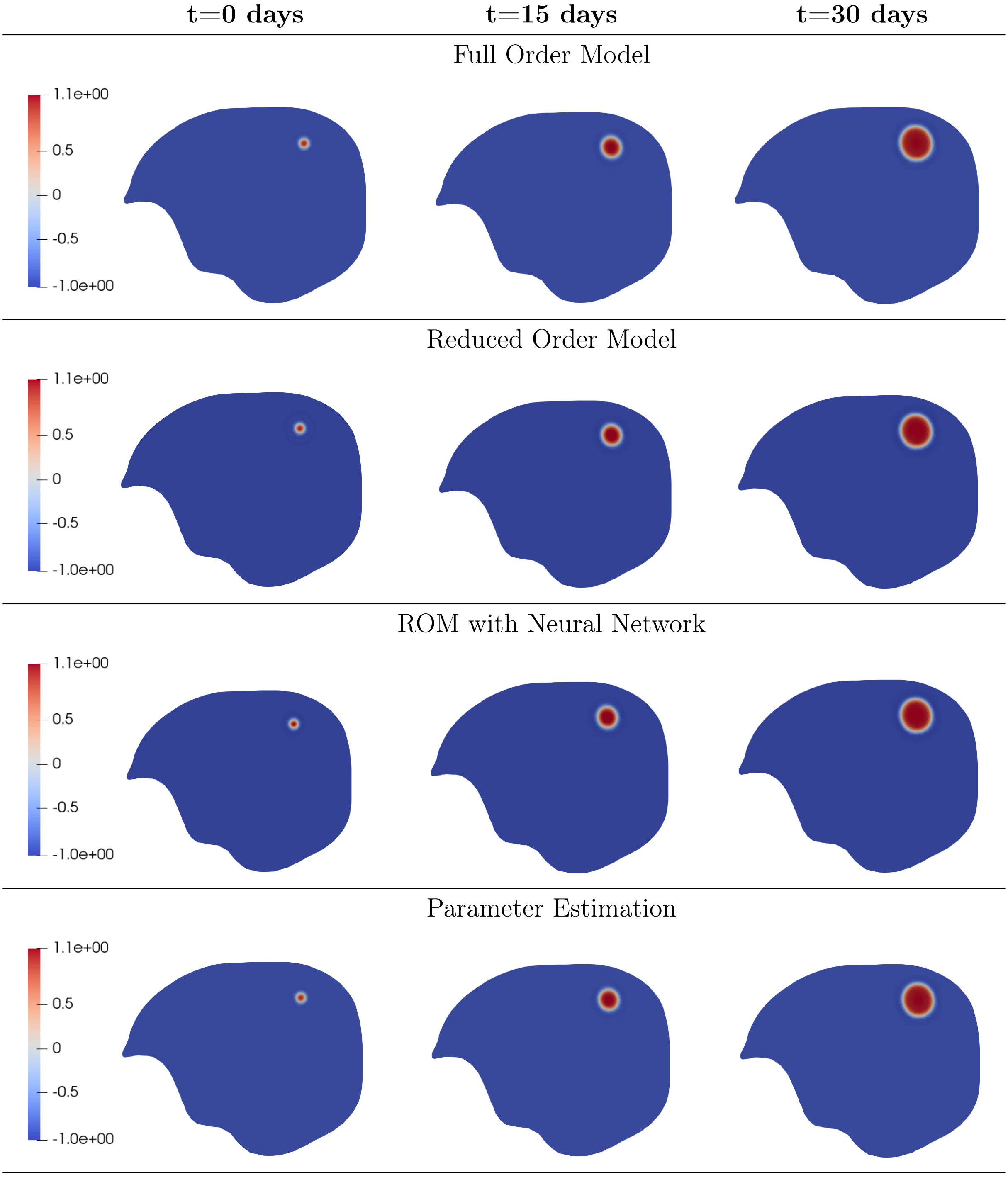

Table 5.8: Evolution of a GMB. From left to right, the solution ϕ for each used method at t$=0, 15, 30$ days are shown. From top to bottom: the solution computed via the Full Order Model; the solution computed via the classical Proper Orthogonal Decomposition; the solution computed via the Neural Network variation of the POD; the solution computed via FOM starting from the parameter obtained in the inverse problem.

6 | Conclusions

Glioblastoma multiforme (GBM) is one of the most aggressive and complex tumours in the central nervous system, attacking the glial cells. Compared with other types of cancers, it has a very high mortality rate, from 70% to 96% according to the age of the patient and has an incidence of 2-3 new cases per year per 100,000 inhabitants in industrialised countries. Adjuvant therapy is able to slow down the disease progression but it is unable to prevent its recurrence after surgical treatment. For all these reasons, much clinical attention is devoted to designing new therapeutic strategies to fight GBM.

Although discrete, hybrid, and continuous models of GBM growth have been proposed in the mathematical literature, they are not yet clinically applicable due to the difficulty of constructing a patient-specific model that is accurate and predictive enough to aid clinical decision-making.

In this work, we presented a continuous physics-based model and its computational application for simulating the personalized growth and progression of GBM.

The thesis is organized as follows. Chapter 1 is devoted to a presentation of the biological background that is needed to understand the phenomenology of a growing tumour better.

In Chapter 2, various imaging techniques in order to obtain patient-specific data are discussed. It is important to remark that a good estimation of the tumour growth and recurrence depends on a correct mapping of the morphology of the brain tissue, of the tumour shape at a particular instant and of the direction of preferential motility both for the tumour and its nutrient. It is possible, indeed, to retrieve via Diffusion Tensor Imaging (DTI) a patient-specific distribution for the tensors D and T, respectively denoting the diffusion preferential direction and the areas where the tumour grows faster, extracted with a multi-compartment algorithm.

In Chapter 3, we construct the mathematical model of GBM growth. The Cahn-Hilliard type equation used to describe the tumour concentration distribution implies some nonlinear terms that make the Full Order Model (FOM) expensive from a computational point of view. For the solution of the full order PDEs system, we make use of `FEniCSx`, a powerful open-source computing platform. The implementation of the used code heavily relies on two of its components: `Dolfinx`, a C++/Python library providing data structures and algorithms for finite element meshes, automated finite element assembly, and numerical linear algebra and Unified Form Language `UFL` which is a domain-specific language for declaration of finite element discretizations of variational forms.

To reduce the degrees of freedom of the problem it is possible to find in literature different techniques. Here, we have studied the impact of the Proper Orthogonal Decomposition method in the construction of the Reduced Order Model (ROM), which reduces the dimensionality of a system by transforming the original variables into a new set of uncorrelated variables (called POD modes, or principal components). In this way, the first few modes ideally retain most of the energy present in all of the original variables. Thus, it is possible to cut down the number of degrees of freedom (d.o.f) from thousands d.o.f (32293 for the brain mesh presented in Chapter 5) to tens d.o.f (40 as showed in Section 5.3.1).

The Full Order Model reduction is computed thanks to the C++/Python library `RBniCSx` [36] that contains a set of functions for performing several reduced order modelling techniques.

As we can see from the results, without the usage of a discrete empirical interpolation method, which has to be appropriately adapted in order to deal with highly nonlinear parabolic partial differential equations, the resolution of a ROM is actually more demanding from a computational standpoint, taking almost 7-8 times more computational effort in terms of elapsed time (see Table 5.7).

In this work, we propose an alternative approach that relies on the power of the Neural Networks (NN) to cut computational costs after proper training. Indeed coupling the POD method for constructing the basis with a neural network (POD-NN) to map the space of the parameters into the space of the coefficient for the reduced order basis, we move all the computational effort at the starting analysis of the tumour evolution. In such a way, we have built up a network that predicts all the possible evolutions from a physiological point of view. The gain, in terms of computational time, is about 100:1 when we compare the elapsed time for computing the reduced solution using POD and its NN-based variation, once the training is performed.

This simplification is of primary importance when we want to perform an estimation of patient-specific parameters. The reduction of the degrees of freedom is, in fact, essential to the construction of a second simple neural network that allows predicting the parameters from a pair of snapshots distant in time. Indeed, we rely on a map that goes from the space of the pairs of reduced coefficients of the solution to the space of parameters. From the training phase of this network, we obtain a relative mean square error of about 15% on the parameters prediction, for the realistic domain case. This result seems not to affect the difference between the actual and predicted evolution.

The computational effort of the simulations phase, which can start as soon as we get information on the actual status of the patient and which includes enough simulation to train the neural networks, is balanced by the rapidity of a patient-specific prediction once we collect a second piece of information on the evolution of the tumour growth. The elapsed time for the estimation of the parameters is indeed of the order of seconds ($5\,s$ in our simulations) since it only requests the evaluation of the trained map at a specific point given by the projected couple of snapshots onto the ROM space.

In a real clinical case, thus, starting from a first image of the actual status of the patient, we can retrace all the steps previously described in order to set a predicted growth, specific to the patient, once a second image is obtained.

Future developments in the approach presented in this work can be the addition in the mathematical model of factors taking into account the adjuvant therapy. Moreover, since this method is heavily dependent on the initial conditions and on the used mesh geometry, another interesting evolution could be the creation of a data set able to map the patient-specific parameters over different initial conditions and mesh geometries without re-training networks for each patient.

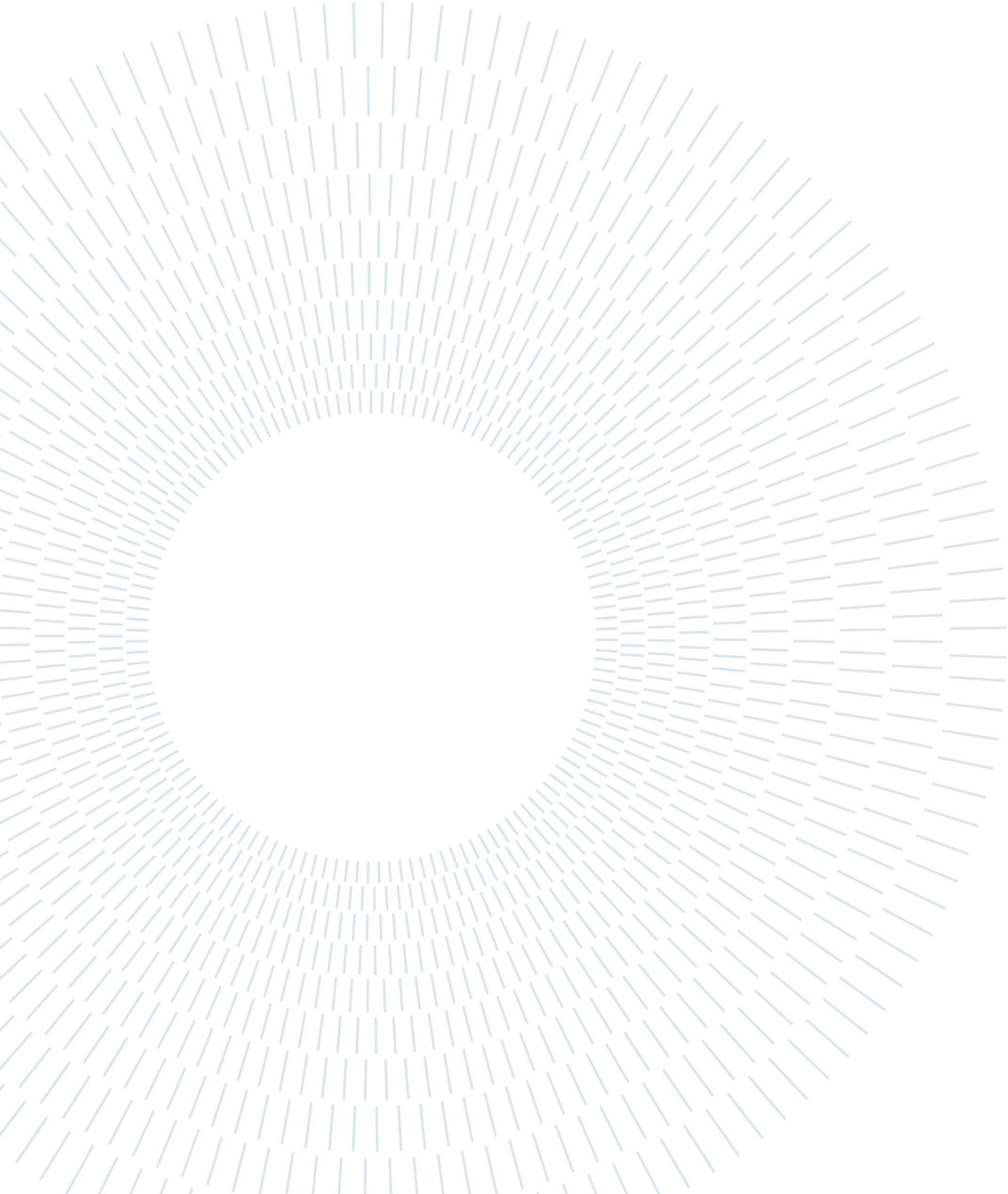

Bibliography

[1] `DOLFINx`. URL `https://github.com/FEniCS/dolfinx`.

[2] Unified form language (ufl). URL `https://github.com/FEniCS/ufl`.

[3] brain stem, . URL `https://en.wiktionary.org/wiki/brain_stem`.

[4] Gray and white matter, . URL `https://www.ncbi.nlm.nih.gov/books/NBK553239/figure/article-36416.image.f1/`.

[5] Magnetic resonance imaging (mri), principi fisici di formazione del segnale e di acquisizione delle immagini. URL `http://www.dmf.unisalento.it/~denunzio/allow_listing/CORSO_TIDM/Presentazione_benedetta_tafuri_mri.pdf`.

[6] Leakyrelu. URL `https://pytorch.org/docs/stable/generated/torch.nn.LeakyReLU.html`.

[7] White matter fiber architecture from the connectome scanner dataset., . URL `http://humanconnectomeproject.org`.

[8] Case western reserve university school of medicine., . URL `http://casemed.case.edu/clerkships/neurology/NeurLrngObjectives/MRI.htm`.

[9] A. Agosti, C. Cattaneo, C. Giverso, D. Ambrosi, and P. Ciarletta. A computational framework for the personalized clinical treatment of glioblastoma multiforme. *ZAMM - Journal of Applied Mathematics and Mechanics / Zeitschrift für Angewandte Mathematik und Mechanik*, 98(12):2307–2327, 2018. doi: https://doi.org/10.1002/zamm.201700294. URL `https://onlinelibrary.wiley.com/doi/abs/10.1002/zamm.201700294`.

[10] A. Agosti, P. Ciarletta, H. Garcke, and M. Hinze. Learning patient-specific parameters for a diffuse interface glioblastoma model from neuroimaging data. *Mathematical Methods in the Applied Sciences*, 43(15):8945–8979, 2020.

[11] B. Alberts. *Molecular biology of the cell*. Garland Publishing, New York, NY, 6 edition, Nov. 2014.

[12] D. Ambrosi and L. Preziosi. On the closure of mass balance models for tumor growth. *Mathematical Models and Methods in Applied Sciences*, 12:737–754, 2002.

[13] G. A. Ateshian. On the theory of reactive mixtures for modeling biological growth. *Biomechanics and modeling in mechanobiology*, 6:423–445, 2007.

[14] B. Bedogni and M. B. Powell. Hypoxia, melanocytes and melanoma–survival and tumor development in the permissive microenvironment of the skin. *Pigment cell & melanoma research*, 22(2):166–174, 2009.

[15] J. Bell. Fréchet derivatives and gâteaux derivatives. *Department of Mathematics*, 2014.

[16] H. Byrne and L. Preziosi. Modelling solid tumour growth using the theory of mixtures. *Mathematical medicine and biology: a journal of the IMA*, 20(4):341–366, 2003.

[17] G. Castaneda, P. Morris, and T. Khoshgoftaar. Evaluation of maxout activations in deep learning across several big data domains. *Journal of Big Data*, 6, 08 2019. doi: 10.1186/s40537-019-0233-0.

[18] C. Chatelain, T. Balois, P. Ciarletta, and M. B. Amar. Emergence of microstructural patterns in skin cancer: a phase separation analysis in a binary mixture. *New Journal of Physics*, 13(11):115013, 2011.

[19] O. Clatz, M. Sermesant, P.-Y. Bondiau, H. Delingette, S. K. Warfield, G. Malandain, and N. Ayache. Realistic simulation of the 3-d growth of brain tumors in mr images coupling diffusion with biomechanical deformation. *IEEE transactions on medical imaging*, 24(10):1334–1346, 2005.

[20] V. Cristini, H. B. Frieboes, R. Gatenby, S. Caserta, M. Ferrari, and J. Sinek. Morphologic instability and cancer invasion. *Clinical Cancer Research*, 11(19):6772–6779, 2005.

[21] G. Cybenko. Continuous valued neural networks with two hidden layers are sufficient, department of computer science. *Trfts. University*, 31, 1988.

[22] G. Cybenko. Approximation by superpositions of a sigmoidal function. *Mathematics of control, signals and systems*, 2(4):303–314, 1989.

[23] M. E. Davis. Glioblastoma: Overview of disease and treatment. *Clin. J. Oncol. Nurs.*, 20(5):S2–8, Oct. 2016.

[24] L. M. DeAngelis and P. Y. Wen. *Primary and Metastatic Tumors of the Nervous*

System. McGraw-Hill Education, New York, NY, 2022. URL `accessmedicine.mhmedical.com/content.aspx?aid=1198036521`.

[25] T. Deisboeck, Z. Wang, P. Macklin, and V. Cristini. Multiscale cancer modeling. *Annual review of biomedical engineering*, 13, 07 2010. doi: 10.1146/annurev-bioeng-071910-124729.

[26] M. Epstein. *The elements of continuum biomechanics*. John Wiley & Sons, 2012.

[27] F. B. Furnari, T. Fenton, R. M. Bachoo, A. Mukasa, J. M. Stommel, A. Stegh, W. C. Hahn, K. L. Ligon, D. N. Louis, C. Brennan, L. Chin, R. A. DePinho, and W. K. Cavenee. Malignant astrocytic glioma: genetics, biology, and paths to treatment. *Genes Dev.*, 21(21):2683–2710, Nov. 2007.

[28] M. L. Goodenberger and R. B. Jenkins. Genetics of adult glioma. *Cancer Genet.*, 205(12):613–621, Dec. 2012.

[29] M. E. Gurtin. Generalized ginzburg-landau and cahn-hilliard equations based on a microforce balance. *Physica D: Nonlinear Phenomena*, 92(3-4):178–192, 1996.

[30] D. Hanahan and R. Weinberg. Hallmarks of cancer: The next generation. *Cell*, 144(5):646–674, 2011. ISSN 0092-8674. doi: https://doi.org/10.1016/j.cell.2011.02.013. URL `https://www.sciencedirect.com/science/article/pii/S0092867411001279`.

[31] D. Hanahan and R. A. Weinberg. The hallmarks of cancer. *Cell*, 100(1):57–70, Jan. 2000.

[32] H. L. P. Harpold, E. C. Alvord, Jr, and K. R. Swanson. The evolution of mathematical modeling of glioma proliferation and invasion. *J. Neuropathol. Exp. Neurol.*, 66(1): 1–9, Jan. 2007.

[33] H. Hatzikirou, A. Deutsch, C. Schaller, M. Simon, K. Swanson, N. Bellomo, and P. Maini. Mathematical modelling of glioblastoma tumour development: A review. *Mathematical Models and Methods in Applied Sciences*, 24:1779–1794, 11 2005. doi: 10.1142/S0218202505000960.

[34] S. Herculano-Houzel. The human brain in numbers: a linearly scaled-up primate brain. *Front. Hum. Neurosci.*, 3:31, Nov. 2009.

[35] J. Hesthaven and S. Ubbiali. Non-intrusive reduced order modeling of nonlinear problems using neural networks. *Journal of Computational Physics*, 363, 02 2018. doi: 10.1016/j.jcp.2018.02.037.

[36] J. S. Hesthaven, G. Rozza, and B. Stamm. *Certified Reduced Basis Methods for Parametrized Partial Differential Equations*. SpringerBriefs in Mathematics. Springer International Publishing, 2015. ISBN 978-3-319-22469-5.

[37] R. K. Hobbie and B. J. Roth. Sound and ultrasound. In *Intermediate Physics for Medicine and Biology*, pages 343–357. Springer New York, New York, NY, 2007.

[38] W. L. Kemp, D. K. Burns, and T. G. Brown. *Chapter 4. Neoplasia*. The McGraw-Hill Companies, New York, NY, 2008. URL `accessmedicine.mhmedical.com/content.aspx?aid=57050916`.

[39] P. Kleihues, D. N. Louis, B. W. Scheithauer, L. B. Rorke, G. Reifenberger, P. C. Burger, and W. K. Cavenee. The WHO classification of tumors of the nervous system. *J. Neuropathol. Exp. Neurol.*, 61(3):215–25; discussion 226–9, Mar. 2002.

[40] A. Martínez-González, G. F. Calvo, L. A. Pérez Romasanta, and V. M. Pérez-García. Hypoxic cell waves around necrotic cores in glioblastoma: a biomathematical model and its therapeutic implications. *Bulletin of mathematical biology*, 74:2875–2896, 2012.

[41] J. Merodio and R. Ogden. Basic equations of continuum mechanics. In *Constitutive Modelling of Solid Continua*, Solid mechanics and its applications, pages 1–16. Springer International Publishing, Cham, 2020.

[42] J. Morales. A numerical study of limited memory bfgs methods. *Applied Mathematics Letters*, 15(4):481–487, 2002. ISSN 0893-9659. doi: https://doi.org/10.1016/S0893-9659(01)00162-8. URL `https://www.sciencedirect.com/science/article/pii/S0893965901001628`.

[43] S. Mori. In S. Mori, editor, *Introduction to Diffusion Tensor Imaging*. Elsevier Science B.V., Amsterdam, 2007. ISBN 978-0-444-52828-5. doi: https://doi.org/10.1016/B978-044452828-5/50025-9. URL `https://www.sciencedirect.com/science/article/pii/B9780444528285500259`.

[44] Q. T. Ostrom, H. Gittleman, J. Fulop, M. Liu, R. Blanda, C. Kromer, Y. Wolinsky, C. Kruchko, and J. S. Barnholtz-Sloan. CBTRUS statistical report: Primary brain and central nervous system tumors diagnosed in the united states in 2008-2012. *Neuro. Oncol.*, 17 Suppl 4(suppl 4):iv1–iv62, Oct. 2015.

[45] G. Powathil, M. Kohandel, S. Sivaloganathan, A. Oza, and M. Milosevic. Mathematical modeling of brain tumors: effects of radiotherapy and chemotherapy. *Physics*

in Medicine & Biology, 52(11):3291, may 2007. doi: 10.1088/0031-9155/52/11/023. URL `https://dx.doi.org/10.1088/0031-9155/52/11/023`.

[46] G. Pozzi, B. Grammatica, L. Chaabane, M. Catucci, A. Mondino, P. Zunino, and P. Ciarletta. T cell therapy against cancer: A predictive diffuse-interface mathematical model informed by pre-clinical studies. *Journal of Theoretical Biology*, 547: 111172, 2022. ISSN 0022-5193. doi: https://doi.org/10.1016/j.jtbi.2022.111172. URL `https://www.sciencedirect.com/science/article/pii/S0022519322001709`.

[47] A. Quarteroni and S. Quarteroni. *Numerical models for differential problems*, volume 2. Springer, 2009.

[48] V. Ramanuj, R. Sankaran, and B. Radhakrishnan. A sharp interface model for deterministic simulation of dendrite growth. *Computational Materials Science*, 169: 109097, 2019.

[49] S. Ratti, M. V. Marvi, S. Mongiorgi, E. O. Obeng, I. Rusciano, G. Ramazzotti, L. Morandi, S. Asioli, M. Zoli, D. Mazzatenta, P.-G. Suh, L. Manzoli, and L. Cocco. Impact of phospholipase c $\beta 1$ in glioblastoma: a study on the main mechanisms of tumor aggressiveness. *Cellular and Molecular Life Sciences*, 79(4):195, Mar 2022. ISSN 1420-9071. doi: 10.1007/s00018-022-04198-1. URL `https://doi.org/10.1007/s00018-022-04198-1`.

[50] M. Á. Rodríguez Bellido, F. M. Guillén González, and G. Tierra Chica. Numerical methods for solving the cahn-hilliard equation and its applicability to mixtures of isotropic and nematic flows with anchoring effects. *Mixing and Mixtures in Geo-and Biophysical Flows: A Focus on Mathematical Theory and Numerical Methods 2016 (2016), pp. 1-68.*, 2016.

[51] C. Sarkar, A. Jain, and V. Suri. Current concepts in the pathology and genetics of gliomas. *Indian J. Cancer*, 46(2):108–119, Apr. 2009.

[52] R. Stupp, M. Gander, S. Leyvraz, and E. Newlands. Current and future developments in the use of temozolomide for the treatment of brain tumours. *Lancet Oncol.*, 2(9): 552–560, Sept. 2001.

[53] R. Stupp, W. P. Mason, M. J. Van Den Bent, M. Weller, B. Fisher, M. J. Taphoorn, K. Belanger, A. A. Brandes, C. Marosi, U. Bogdahn, et al. Radiotherapy plus concomitant and adjuvant temozolomide for glioblastoma. *New England journal of medicine*, 352(10):987–996, 2005.

[54] B. Sundén. Chapter 9 - transport phenomena in fuel cells. In

B. Sundén, editor, *Hydrogen, Batteries and Fuel Cells*, pages 145–166. Academic Press, 2019. ISBN 978-0-12-816950-6. doi: https://doi.org/10.1016/B978-0-12-816950-6.00009-9. URL `https://www.sciencedirect.com/science/article/pii/B9780128169506000099`.

[55] H. Sung, J. Ferlay, R. L. Siegel, M. Laversanne, I. Soerjomataram, A. Jemal, and F. Bray. Global cancer statistics 2020: Globocan estimates of incidence and mortality worldwide for 36 cancers in 185 countries. *CA: A Cancer Journal for Clinicians*, 71(3):209–249, 2021. doi: https://doi.org/10.3322/caac.21660. URL `https://acsjournals.onlinelibrary.wiley.com/doi/abs/10.3322/caac.21660`.

[56] E. A. Swabb, J. Wei, and P. M. Gullino. Diffusion and convection in normal and neoplastic tissues. *Cancer research*, 34(10):2814–2822, 1974.

[57] K. R. Swanson, E. C. Alvord Jr, and J. Murray. A quantitative model for differential motility of gliomas in grey and white matter. *Cell proliferation*, 33(5):317–329, 2000.

[58] S. Torabi, S. Wise, J. Lowengrub, A. Rätz, and A. Voigt. A new method for simulating strongly anisotropic cahn-hilliard equations. 3, 01 2007.

[59] S. Wise, J. Lowengrub, H. Frieboes, and V. Cristini. Three-dimensional multispecies nonlinear tumor growth—i: Model and numerical method. *Journal of Theoretical Biology*, 253(3):524–543, 2008. ISSN 0022-5193. doi: https://doi.org/10.1016/j.jtbi.2008.03.027. URL `https://www.sciencedirect.com/science/article/pii/S0022519308001525`.

[60] R. M. Young, A. Jamshidi, G. Davis, and J. H. Sherman. Current trends in the surgical management and treatment of adult glioblastoma. *Ann. Transl. Med.*, 3(9): 121, June 2015.

List of Figures

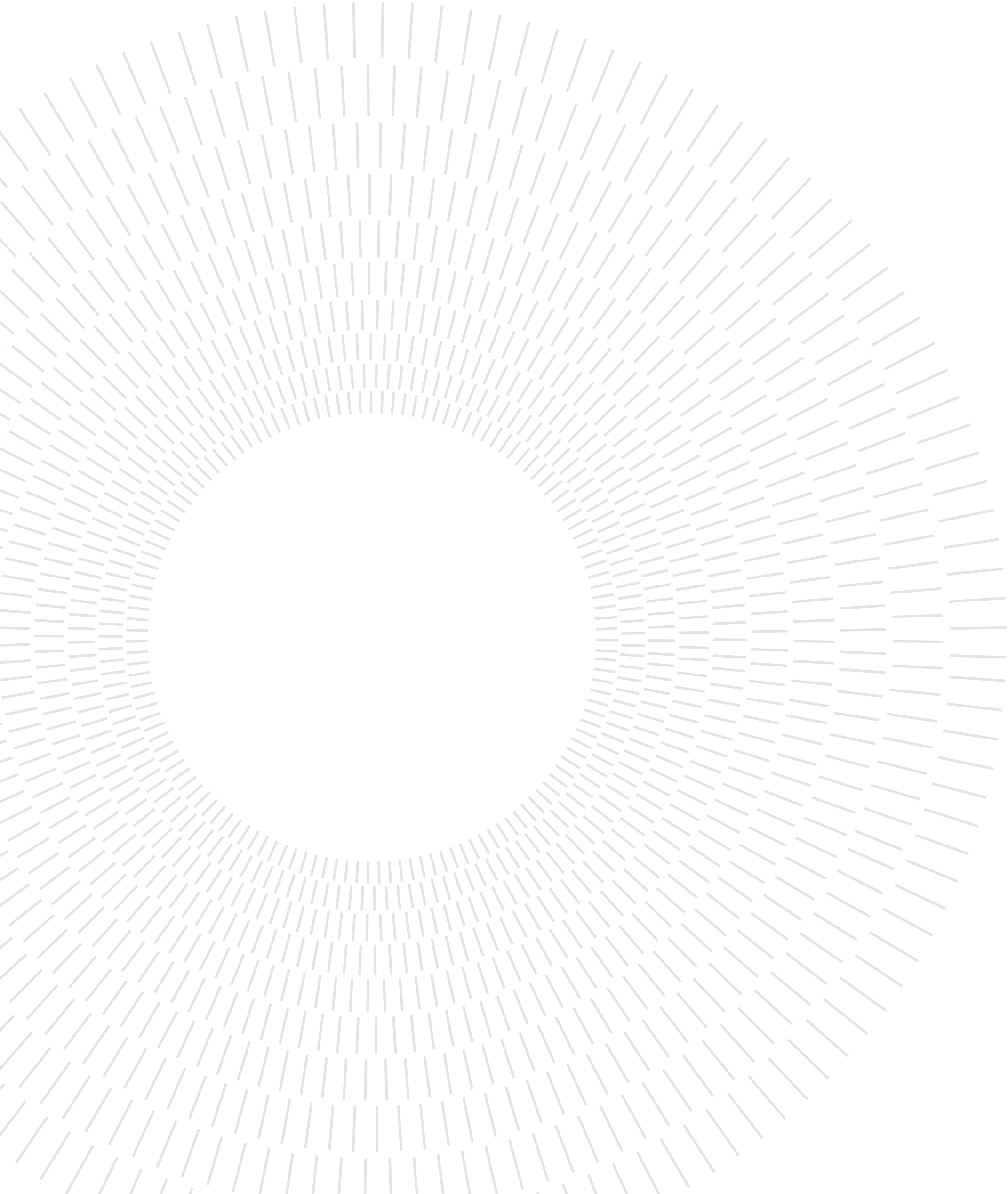

List of Tables

Ringraziamenti

Un ringraziamento speciale va al mio relatore, il professore Pasquale Ciarletta, non solo per avermi dato la possibiltà di lavorare su un tema che mi appassiona da sempre ma per essermi stato di costante supporto e stimolo durante questo progetto. Un grazie sincero va anche al professore Paolo Zunino che è stato di grandissimo aiuto per oltrepassare gli ostacoli che si sono presentati nelle varie strade che abbiamo provato a percorrere. Un immenso grazie al dottor Davide Riccobelli, fondamentale nel raggiungimento dei risultati ottenuti, che oltre a dispensare utili consigli è stato di grandissima disponibilità e sostegno. Ringrazio poi il dottor Francesco Ballarin che mi ha dato la possibilità di utilizzare la sua libreria per i metodi a basi ridotte e che mi ha giudato nell'apprendimento delle sue funzionalità. Un grazie va anche al professor Andrea Manzoni per il suo preziosissimo apporto nella costruzione del modello ridotto.